CHALMERS
UNIVERSITY OF TECHNOLOGY

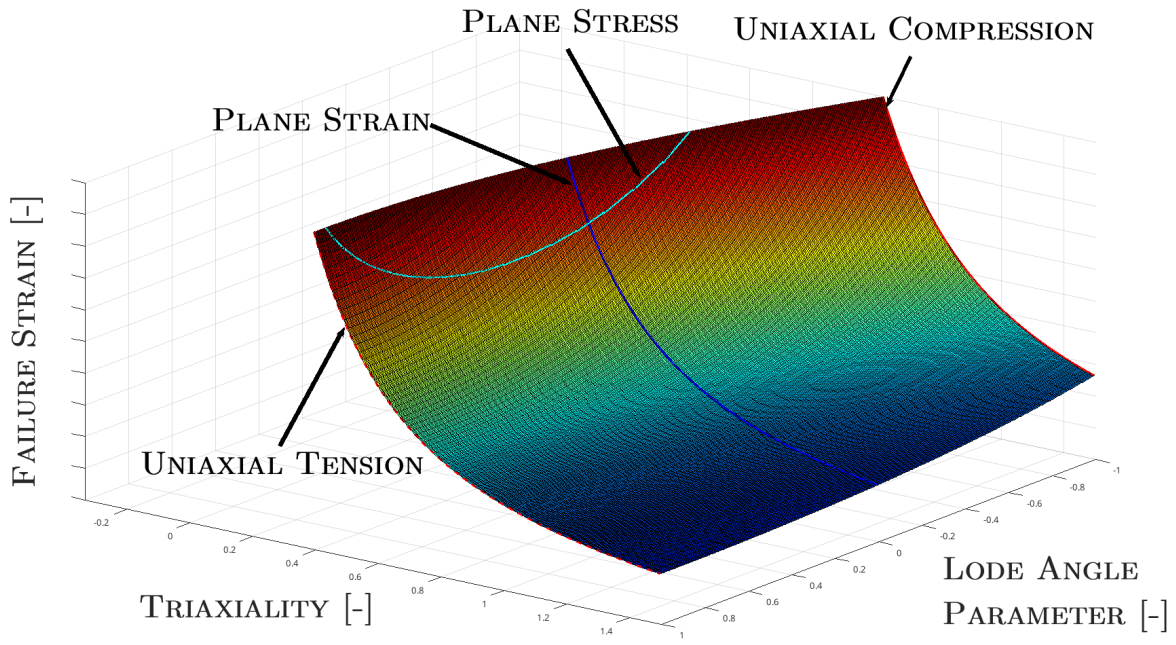

Verification of Plane Stress Material Model Behaviour in Solid 3D-Structures

Master's thesis in Applied Mechanics

OWEIS AL-KARAWI
VICTOR MATHIESEN

DEPARTMENT OF INDUSTRIAL AND MATERIALS SCIENCE

CHALMERS UNIVERSITY OF TECHNOLOGY
Gothenburg, Sweden 2024
www.chalmers.se

Master's thesis 2024

Verification of Plane Stress Material Model Behaviour in Solid 3D-Structures

OWEIS AL-KARAWI
VICTOR MATHIESEN

CHALMERS
UNIVERSITY OF TECHNOLOGY

Department of Industrial and Materials Science
Chalmers University of Technology
Gothenburg, Sweden 2024

Verification of Plane Stress Material Model Behaviour in Solid 3D-Structures

OWEIS AL-KARAWI
VICTOR MATHIESEN

© OWEIS AL-KARAWI, 2024.
© VICTOR MATHIESEN, 2024.

Supervisor: Per-Anders Eggertsen, Volvo Cars Corporation
Supervisor: Johan Jergeus, Volvo Cars Corporation
Examiner: Martin Fagerström, Department of Industrial and Materials Science

Master's Thesis 2024
Department of Industrial and Materials Science
Chalmers University of Technology
SE-412 96 Gothenburg
Telephone +46 31 772 1000

Cover: An example of a failure surface with pointers to different important parts.

Typeset in LaTeX
Printed by Chalmers Reproservice
Gothenburg, Sweden 2024

Verification of Plane Stress Material Model Behaviour in Solid 3D Structures
OWEIS AL-KARAWI
VICTOR MATHIESEN
Department of Industrial and Materials Science
Chalmers University of Technology

Abstract

In the automotive industry, car crash simulations are an important tool to use in the development process. To accurately capture material behaviour, a well-calibrated material failure model must be used. Volvo Cars Corporation is currently using an advanced material failure model called "MF GenYld + CrachFEM" which is calibrated for the use of shell elements. However, in recent years there has been an increasing interest for the use of 3D solid elements.

The main objective of this project is to assess the CrachFEM model to evaluate its suitability for the use of 3D solid elements by comparing LS-DYNA simulations of both shells and solids to physical tests. Additionally, the CrachFEM model is compared to another material damage model called GISSMO. Also, with different feasible alternatives to CrachFEM such as the Cockcroft-Latham and modified Mohr-Coloumb failure criteria. Assessments are made on three levels of analysis, which are ordered in increased complexity. The first level is single element simulations, the second level tests coupon simulations, and the third level is component simulations.

The results of the project indicate that CrachFEM is very limited when it comes to solid elements, and further use of the material damage model GISSMO might be beneficial, since it offers much more flexibility and options for calibration to capture experimental data more accurately with solid elements.

Keywords: CrachFEM, GISSMO, Triaxiality, Lode angle parameter, Failure strain, Hardening, Shell elements, Solid elements, Plane stress, Necking

Acknowledgements

First and foremost, we would like to express our deepest gratitude to our main supervisor, Per-Anders, for his support, guidance, and insightful feedback throughout the course of this project. His expertise and dedication have been instrumental in shaping the direction and quality of this work.

We are also grateful to our co-supervisor, Johan Jergeus, for his constructive suggestions, and for always being available to discuss ideas and provide thoughtful insights. His contributions have greatly enhanced the depth and clarity of this research.

A special thanks to Mats Landervik, Johann Körbelin, and Renaud Gutkin at Volvo Cars, whose technical assistance, collaborative spirit, and practical insights have been crucial in the development and execution of this project. Their support and willingness to share their expertise have been immensely appreciated.

We would like to extend our thanks to Martin Fagerström, our examiner, for his meticulous evaluation, insightful comments, and for ensuring the highest standards in this research. His thorough assessment has been vital in refining and finalizing this work.

Additionally, we would like to extend our thanks to all our colleagues at Volvo Cars, who have contributed in various ways to this project. Your encouragement and professional input have made this journey both productive and enjoyable.

Thank you all for your invaluable contributions and support.

Oweis Al-Karawi & Victor Mathiesen
Gothenburg, June 2024

Contents

1 Introduction **3**
- 1.1 Objectives . . . 4
- 1.2 Delimitations . . . 5
- 1.3 Resources . . . 5

2 Theory **7**
- 2.1 Preliminaries . . . 7
  - 2.1.1 Stress State in Three Dimensions . . . 7
  - 2.1.2 Stress Triaxiality . . . 9
  - 2.1.3 Lode Parameter . . . 10
  - 2.1.4 Stages of Deformation . . . 12
- 2.2 Plastic Anisotropy & Fracture Anisotropy . . . 13
- 2.3 FEM in LS-DYNA . . . 14
  - 2.3.1 Explicit Time Integration . . . 15
- 2.4 Material Failure Model CrachFEM . . . 16
  - 2.4.1 Ductile Normal Fracture . . . 17
  - 2.4.2 Ductile Shear Fracture . . . 18
  - 2.4.3 Instability Fracture . . . 20
- 2.5 Lode Dependent Instability . . . 22
- 2.6 Cockcroft-Latham . . . 23
- 2.7 Modified Mohr-Coulomb . . . 23
- 2.8 GISSMO . . . 24

3 Methods **27**
- 3.1 Hardening Curve Effect . . . 27
- 3.2 CrachFEM . . . 27
  - 3.2.1 Single Element Simulation . . . 27
  - 3.2.2 Coupons in Tension . . . 28
- 3.3 GISSMO . . . 33
  - 3.3.1 Sanity Check . . . 33
  - 3.3.2 Plastic Anisotropy with GISSMO . . . 34
  - 3.3.3 Regularization . . . 34
  - 3.3.4 Incorporating Instability for 3D Solids & Studying the Effect of Damage and Fade Exponents . . . 35
  - 3.3.5 Cockcroft-Latham & Modified Mohr-Coulomb Using GISSMO 35
- 3.4 Component Simulation . . . 37

4 Results & Discussion **39**
4.1 Hardening Curve Effect 39
4.2 CrachFEM 41
4.2.1 Single Element Simulation 41
4.2.2 Coupons in Tension 42
4.3 GISSMO 52
4.3.1 Sanity Check 52
4.3.2 Anisotropic Material with GISSMO 53
4.3.3 Regularization 54
4.3.4 Studying the Effect of Damage and Fade Exponent & Incorporating Instability for 3D Solids 55
4.3.5 Cockcroft-Latham Using GISSMO 60
4.3.6 Modified Mohr-Coulomb Using GISSMO 62
4.4 Component Simulation 63

5 Conclusion & Future Work **67**

Bibliography **69**

1

Introduction

The utilization of aluminium in the automotive industry has become a common trend due to stricter emission targets since the replacement of steel in vehicles achieves both weight loss without affecting safety [1], and reductions in carbon dioxide emissions. By changing the body panels from steel to aluminium, the weight is reduced by about 40% [1]. While the production expense of aluminium surpasses that of steel, the energy savings it offers can contribute to a favourable impact on the total lifetime usage costs [2].

However, the geometrical characteristics of aluminium are different from that of steel, since the aluminium is thicker than the welded steel parts. Furthermore, 3D solid elements can be used to model every kind of structure, it is costly in terms of meshing and it uses more computer power. So for shells, plates, and beams, the usage of more simple kinds of elements is more convenient [3], but this is not the case for aluminium. It requires the use of 3D solid elements in Computer-Aided Engineering (CAE) instead of shell elements, which creates a necessity for investigation of the plane stress assumption that the shells use. However, failure of a 3D solid element must be modeled as a function of at least two stress variables. Normally the stress variables chosen are the triaxiality and a stress parameter tied to the deviatoric stress, while the shell elements can be modeled by triaxiality alone.

There are generally two types of manufactured aluminium that are used in industries; extruded aluminium and cast aluminium. There are some differences between the two and in this project the former is used because it is the production type utilized by Volvo Cars Corporation (VCC). Extruded aluminum is ductile and has high strength and can be extruded into more complicated geometries superior to steels [4]. Extruded aluminum demonstrates both plasticity and fracture anisotropy and with the aid of advanced technology, now allows for the creation of closed sections with variable thickness. This advancement significantly enhances the material's versatility and effectiveness in various applications, particularly in the automotive industry. The remarkable bendability of extruded aluminum facilitates superior energy absorption during crashes, leading to reduced load transfer and increased occupant safety. This capability marks its importance as a preferred material choice in the automotive industry, where optimizing crashworthiness is outstanding [5].

There were a lot of contributions regarding the development of ductile failure criteria, one of these is made by Cockcroft and Latham [6] who created a model weighted

by maximum principle stress which is transformed furthermore into a space of triaxiality, Lode parameter, and average strain $(\eta, L, \varepsilon_{eq})$. A time after this Bai and Wierzbicki [7] extended the Mohr-Coulomb criterion from brittle to ductile materials, and it was later used for predicting the ductile failure for aluminium alloys and high-strength steels. This criterion is called the Modified Mohr-Coulomb (MMC) criterion. Lou et al. [8] also proposed a ductile failure model based on monitoring the microscopic nucleation growth and they suggested a material space model, the same as in the Cockcroft-Latham criterion $(\eta, L, \varepsilon_{eq})$. These ductile failure criteria were compared and evaluated with experimental data by Lou, Y. and Huh, H. [9] using the least square method, and they found that both MMC and Lou criteria achieved the least amount of error.

1.1 Objectives

The main objective of this project is to assess the CrachFEM material failure model to evaluate its validity for the use of 3D solid elements by comparing LS-DYNA simulations of both shells and solids to physical tests. Additionally, the CrachFEM model is compared to another material damage model called GISSMO with different feasible alternatives to CrachFEM such as the Cockcroft-Latham and modified Mohr-Coulomb failure criteria. Other objectives include:

- Generate an interactive script for reading user-defined material failure models for visualization and comparison of the different failure curves/surfaces.
- Develop CAE-models to compare shell and solid representations for material test configurations (coupons) using continuum elements and investigate how sensitive the FE-model's outcomes are to changes in mesh parameters.
- Compare the different CAE results with test data and the VCC shell material models for verification.
- Gain an understanding of how various components of material cards contribute to discrepancies observed between representations in shell and solid element contexts.

1.2 Delimitations

The following delimitations are set on the project:

- The project does not include the use of material models other than the ones available at VCC.
- The project will be limited to three material failure models; CrachFEM, Cockcroft-Latham, and Modified Mohr-Coulomb Criterion where the last two are implemented in the GISSMO damage model.
- Only one type of extruded aluminium will be used in the analysis, namely 6005A-T6.
- There will be no experimental testing made in the project.

1.3 Resources

Required resources to complete the project:

- Material tests made by Hydro.
- LS-DYNA.
- Material failure models.

2

Theory

This chapter contains a preliminary theory about the stress state of a body in three dimensions, and derived parameters, as well as a theory about FEM in LS-DYNA, what types of failure that occur, and what material failure models are available.

2.1 Preliminaries

Before discussing the theory of failure criteria and the FEM model used for this thesis project, some definitions are necessary for further understanding.

2.1.1 Stress State in Three Dimensions

Consider a three-dimensional body with an external traction acting on it. In any arbitrary point P, the stress state can be described as a stress tensor given that the coordinate system has three normal directions, i.e. x_1, x_2, and x_3, as seen in Fig. 2.1.

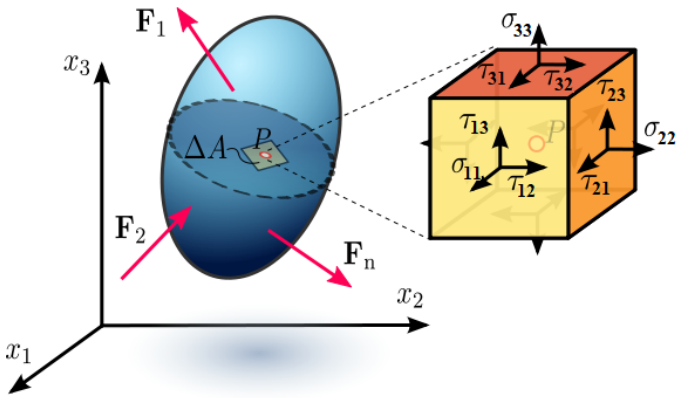

Figure 2.1: Stress tensor components for a three-dimensional body with an arbitrary point P. From [10]. Reproduced and modified with permission.

The stress tensor $\boldsymbol{\sigma}$ can be expressed in matrix form as

$$\boldsymbol{\sigma} = \begin{bmatrix} \sigma_{11} & \tau_{12} & \tau_{13} \\ \tau_{21} & \sigma_{22} & \tau_{23} \\ \tau_{31} & \tau_{32} & \sigma_{33} \end{bmatrix}, \tag{1}$$

where σ are the normal stress components, and τ are the shear stress components.

These nine stress components are shown using a Cartesian coordinate system. If the element was taken at some different orientation but with the same material particle, it would have different tractions acting on it and the stress components would be different. A change of the coordinate system to the axes x_1', x_2', and x_3' can be achieved by using

$$\boldsymbol{\sigma'} = \boldsymbol{A}\boldsymbol{\sigma}\boldsymbol{A}^{\boldsymbol{T}}, \tag{2}$$

where $\boldsymbol{A}$ is the transformation matrix. A visualization of this is shown in Fig. 2.2.

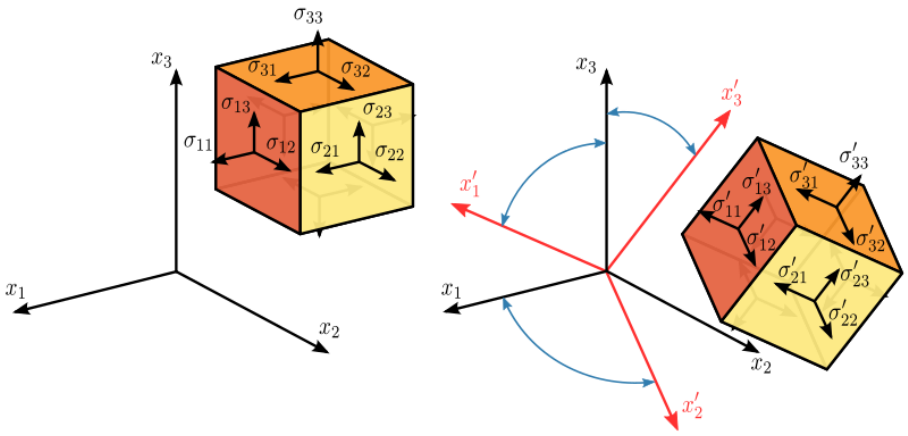

Figure 2.2: Coordinate system transformation for the 3D stress element. From [11]. Reproduced with permission.

The finesse of using a transformed coordinate system comes with principal stresses. Any point in a body subjected to stress has the three principal stresses σ_1, σ_2, and σ_3, and these stresses are the normal stresses present in the transformed coordinate system where all shear stresses are zero.

As stated earlier, the stress components in the stress tensor depend on the orientation of the coordinate system, but as a physical quantity, it has to be independent of whichever coordinate system it is represented in. This means the stress tensor has so-called invariants that do not change with transformations. These invariants are obtained by solving the eigenvalue problem of (2), resulting in the invariants

$$\begin{aligned} I_1 &= tr(\boldsymbol{\sigma}), \\ I_2 &= \frac{1}{2}(tr(\boldsymbol{\sigma})^2 - tr(\boldsymbol{\sigma}^2)), \\ I_3 &= det(\boldsymbol{\sigma}), \end{aligned} \tag{3}$$

where tr is the diagonal sum of the matrix, and det is the determinant.

The stress tensor can further be decomposed into a hydrostatic part and a deviatoric part as

$$\boldsymbol{\sigma} = \boldsymbol{\sigma}_h + \boldsymbol{\sigma}_d = \frac{tr(\boldsymbol{\sigma})}{3}\boldsymbol{I} + \left(\boldsymbol{\sigma} - \frac{tr(\boldsymbol{\sigma})}{3}\boldsymbol{I}\right), \tag{4}$$

where $\boldsymbol{\sigma}_h$ is the hydrostatic stress, $\boldsymbol{I}$ is the identity matrix, and $\boldsymbol{\sigma}_d$ is the deviatoric stress.

Another set of invariants is obtained from the deviatoric part of the stress tensor, resulting in the invariants

$$\begin{aligned} J_1 &= tr(\boldsymbol{\sigma_d}) = 0, \\ J_2 &= \frac{1}{3}I_1^2 - I_2, \\ J_3 &= \frac{2}{27}I_1^3 - \frac{1}{3}I_1 I_2 + I_3 \ . \end{aligned} \tag{5}$$

2.1.2 Stress Triaxiality

The stress triaxiality is a dimensionless parameter defined by some researchers as a parameter that governs the growth of voids [12]. Mathematically, it is used to determine the stress state acting on a body and is defined as

$$\eta = \frac{\sigma_h}{\sigma_{eq}}, \tag{6}$$

where σ_{eq} is the von Mises equivalent stress which is often used as a yield criterion for ductile materials. It has a relation

$$\sigma_{eq} = \sqrt{3J_2} = \sqrt{\frac{(\sigma_1 - \sigma_2)^2 + (\sigma_2 - \sigma_3)^2 + (\sigma_3 - \sigma_1)^2}{2}} \ . \tag{7}$$

The triaxiality parameter is sometimes multiplied with a scale factor or has the sign reversed since no unique expression is defined. However, in this thesis (6) is used to express triaxiality. The triaxiality parameter has defined constant values for some load cases where the plane stress assumption is made, and are presented in Fig 2.3.

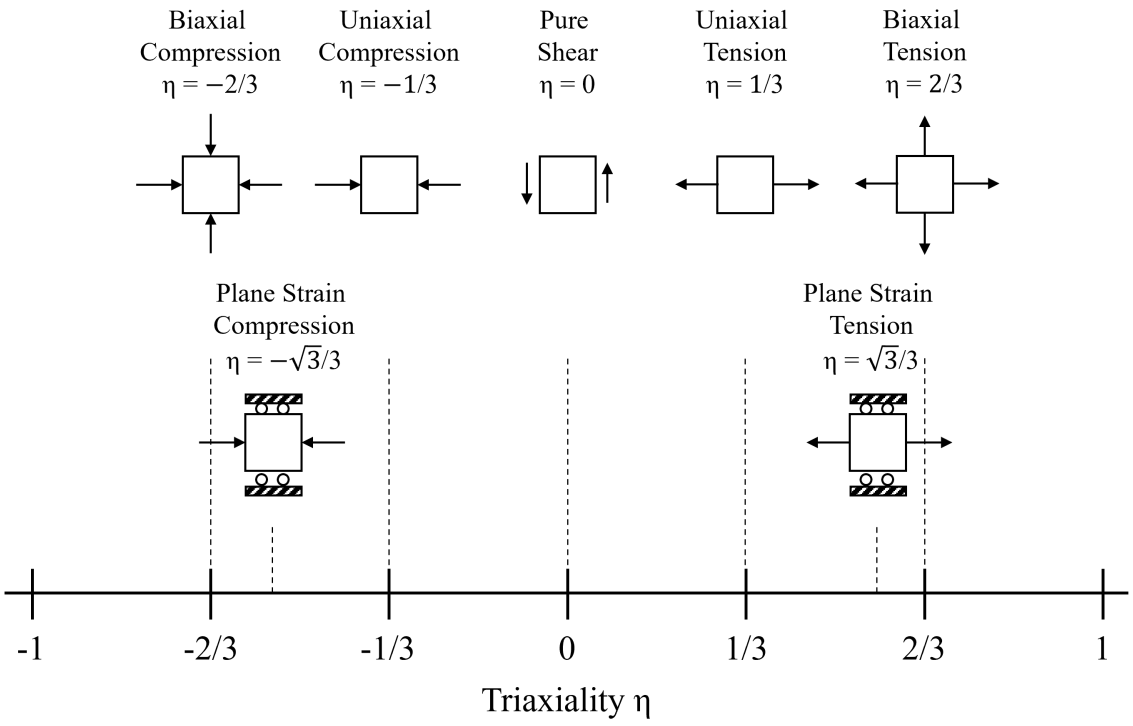

Figure 2.3: Load cases for different values of triaxiality, with the plane stress assumption.

2.1.3 Lode Parameter

It has been shown in studies [13] that both the pressure effect described by the triaxiality parameter and the effect of the third deviatoric stress invariant J_3 should be included when modeling failure strain. This is done by defining the normalized third invariant as

$$\xi = \frac{27}{2}\frac{J_3}{\sigma_{eq}^3} \ . \tag{8}$$

Some researchers define the Lode parameter as a factor governing the formation of void shapes during deformation [12], which is computed as

$$L = \frac{2\sigma_2 - \sigma_1 - \sigma_3}{\sigma_1 - \sigma_3}, \tag{9}$$

and has the range $-1 \leq L \leq 1$. It is related to the normalized third stress invariant as [9]

$$\xi = \cos 3\theta = \frac{L(L-3)(L+3)}{(L^2+3)^{3/2}} \ . \tag{10}$$

The Lode angle θ is defined as the rotation angle of the deviatoric plane around the hydrostatic axis, and the range is $0 \leq \theta \leq \frac{\pi}{3}$ [14]. A visualization of the Lode angle and its range is shown in Fig. 2.4 together with the Tresca and von Mises yield surfaces.

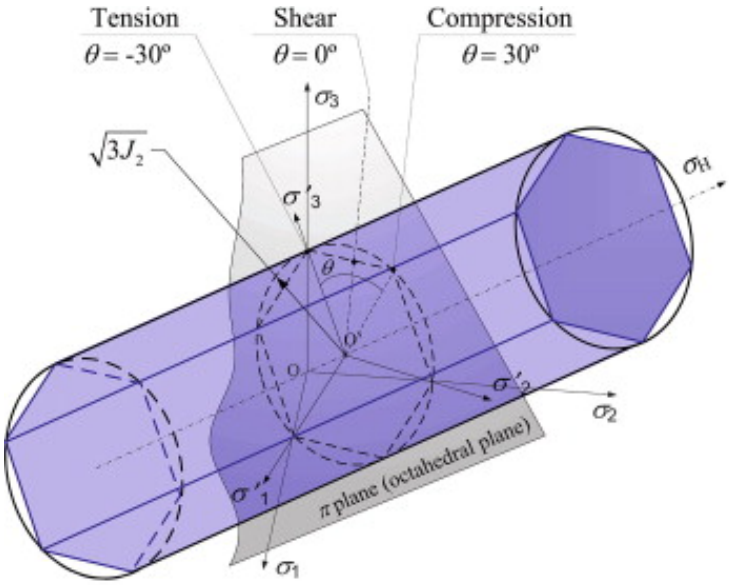

Figure 2.4: Lode angle with Tresca (hexagonal) and von Mises (circular) yield surfaces. From [15]. Reproduced with permission.

The Lode angle can further be normalized into the Lode Angle Parameter (LAP) $\bar{\theta}$ using the expression

$$\bar{\theta} = 1 - \frac{6\theta}{\pi} = 1 - \frac{2}{\pi} \arccos \xi, \tag{11}$$

resulting in a range of $-1 \leq \bar{\theta} \leq 1$. All these parameters are different ways to express the effect of the third deviatoric stress invariant J_3, but in this thesis the LAP $\bar{\theta}$ is chosen as the parameter to be used in further analysis. In Table I three special loading cases and their parametric values are shown [9]. Here it can be seen that the different parameters express the same load cases with different values.

TABLE I
THREE SPECIAL LOADING CASES AND THEIR PARAMETRIC VALUES

Load case	θ	$\bar{\theta}$	L	ξ
Uniaxial tension	0	1	-1	1
Pure shear	$\pi/6$	0	0	0
Uniaxial compression	$\pi/3$	-1	1	-1

2.1.4 Stages of Deformation

Most metals have two types of deformation; elastic and plastic. Elastic deformation is the first region of the stress-strain curve that can be seen in Fig. 2.5 and is a type of deformation that allows the material to return to its original size once external tensile loads are removed. It is governed by Hookes' law, which in 1D is expressed as

$$\sigma = E\varepsilon, \tag{12}$$

where σ is the applied stress, E is the Young's modulus, and ε is the elastic strain.

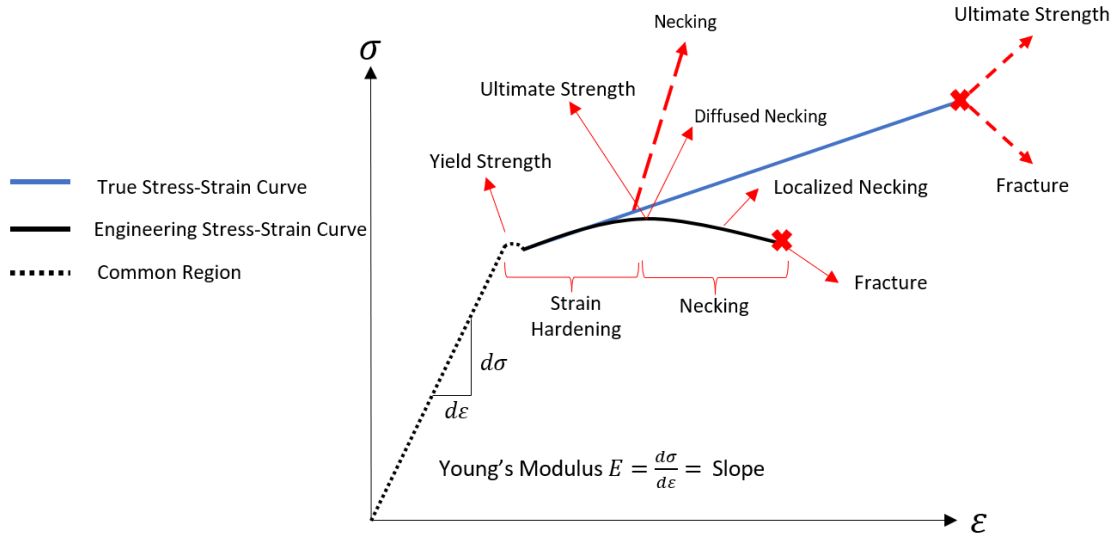

Figure 2.5: Typical stress-strain behaviour of a linear elastic metal. Inspired by [16].

If the external loads exceed the yield strength of the material, the deformation becomes plastic and will result in permanent deformations. This type of deformation is described by a strain-hardening and necking region, which ends in the point of fracture. During strain hardening the material becomes stronger due to dislocations of grains in the metal that work to prevent further deformation. This hardening continues up until a point of ultimate strength when considering engineering stress and strain, where necking begins. The necking phase starts when the material experiences a large local disproportional strain in a small region which results in a local reduction of the cross-sectional area which becomes the exclusive location of additional yielding in the material. An example of how this looks can be seen in Fig. 2.9. At this point, the strain rapidly increases as the strength of the material decreases, and ends at the point of fracture, which is considered the ultimate strength for true stress and strain.

The true stress-strain curve and the engineering stress-strain curve differ significantly in how they represent material deformation. The engineering stress-strain curve uses the original cross-sectional area and length of the material to calculate stress and strain, respectively, which can lead to inaccuracies at higher strains where significant deformation occurs. In contrast, the true stress-strain curve accounts for the actual cross-sectional area and length at any given point during deformation, providing a more accurate representation of the material's behavior under stress. As shown in Fig. 2.5, the true stress-strain curve typically lies above the engineering stress-strain curve after the yield point, reflecting the increasing stress due to the decreasing cross-sectional area of the material under tension.

In this project, Swift hardening model [17] is adopted, which exists in the CrachFEM material card and is governed by

$$\sigma_{eq} = K \cdot (\varepsilon_0 + \varepsilon_{eq})^n, \tag{13}$$

where K, ε_0, and n are material parameters, and ε_{eq} and σ_{eq} are the equivalent strain and stress [18].

2.2 Plastic Anisotropy & Fracture Anisotropy

Plastic anisotropy and fracture anisotropy are two distinct yet critical aspects of material behavior that describe how materials respond differently to stresses and strains depending on the direction. Plastic anisotropy refers to the variation in a material's plastic deformation properties with direction. This phenomenon is prominently observed in metals that have undergone processes like rolling or drawing, which create a preferred grain orientation or microstructural alignment. This directional dependence influences how the material yields and deforms when subjected to external loads, which is crucial in applications such as sheet metal forming. Engineers use plastic anisotropy models, such as the Barlat [19] material model, to predict material behavior during forming processes, ensuring accuracy and efficiency in manufacturing.

In contrast, fracture anisotropy relates to the directional variation in a material's fracture behavior, specifically how cracks initiate and propagate under stress. This property is vital for materials where resistance to crack growth or fracture toughness varies with direction due to the material's microstructure or the presence of aligned defects. Understanding fracture anisotropy enables the design of safer, more reliable structures by predicting potential failure modes and strengths in different loading directions. While plastic anisotropy models predict yielding and plastic flow, fracture anisotropy is analyzed using fracture mechanics approaches that focus on crack growth and resistance.

2.3 FEM in LS-DYNA

While LS-DYNA offers various element types and formulations, it is important to note that the use of triangular shell elements is not advisable in bending problems due to their inherent stiffness as constant strain elements. Consequently, FE-solvers may necessitate a substantial number of triangular elements to effectively capture bending phenomena [20]. Opting for quadratic elements does not eliminate the need for triangular elements, as certain geometries may require a mix of element formulations to accurately fill areas. The main choice of element type is a quadratic element and their formulation is shown in Figure 2.6. Figure 2.7 is a representation of the hexahedron elements and it is an extruded version of the quadratic elements.

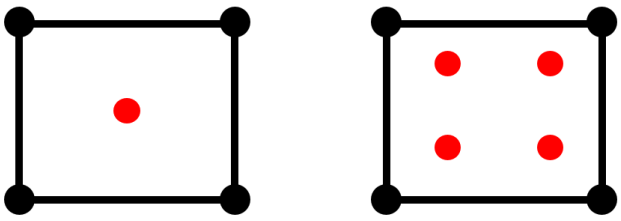

Figure 2.6: Quadratic elements with one integration point in the middle (Left), and four integration points (Right).

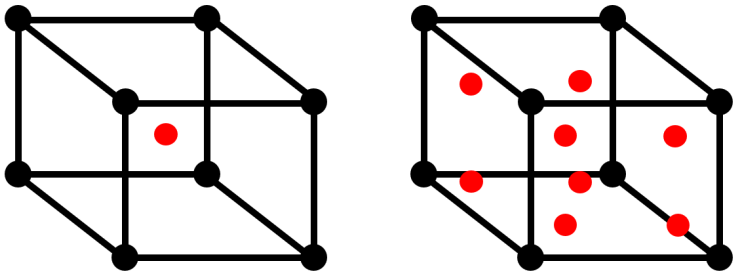

Figure 2.7: Hexahedron elements with one integration point in the middle (Left), and eight integration points (Right).

When modeling with solid elements, generating a hexahedral mesh for complex, curved, or intricate geometries is often highly challenging and typically demands significant manual effort and advanced meshing techniques to achieve a well-fitting, structured mesh. To be able to easily model more complex geometry, the tetrahedron elements are commonly used. A representation of a tetrahedron element is shown in Fig 2.8.

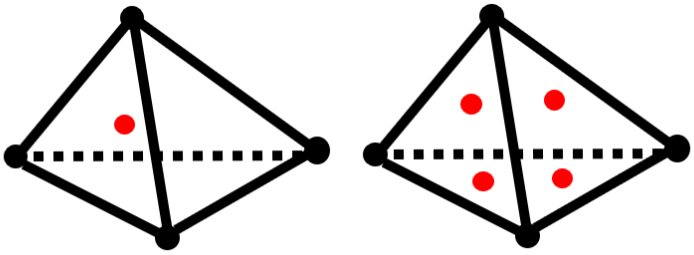

Figure 2.8: Tetrahedron elements with one integration point in the middle (Left), and four integration points (Right).

When building an FEM model, there are some parameters that will greatly affect the outcome of the results. These parameters are mainly the mesh density, i.e. the size of the elements which controls how many elements the model uses. But the type of element and if it uses a linear formulation or a quadratic or higher formulation will also greatly affect the results. For solids it is of a greater importance to have enough integration points through the thickness since the physical properties are captured with the geometry. This is not the case for shell elements since they use the plane stress assumption.

2.3.1 Explicit Time Integration

When solving differential equations with FE-analysis, either an implicit or explicit method is used. In this thesis, it is limited to explicit methods since that is what the CrachFEM model is using. The undamped equation of motion can be written as

$$\boldsymbol{M}\,{}^{n}\ddot{\boldsymbol{a}} + \boldsymbol{f}^{int}({}^{n}\boldsymbol{a}) = {}^{n}\boldsymbol{f}^{ext}, \tag{14}$$

where $\boldsymbol{M}$ is the mass matrix, ${}^{n}\ddot{\boldsymbol{a}}$ are the nodal accelerations, $\boldsymbol{f}^{int}$ are the internal forces, ${}^{n}\boldsymbol{a}$ are the nodal displacements, ${}^{n}\boldsymbol{f}^{ext}$ are the external forces, and index n represents the current time step.

The finesse of using the explicit method is that it solves the system for ${}^{n}\ddot{\boldsymbol{a}}$ instead of ${}^{n}\boldsymbol{a}$, and by doing so avoids inverting a tangent stiffness matrix, which is very computationally heavy. The Newmark's time integration scheme can be used to solve (14) for ${}^{n}\ddot{\boldsymbol{a}}$ [21] which reduces the integration scheme to

$${}^{n+1}\boldsymbol{a} = {}^{n}\boldsymbol{a} + \Delta t\,{}^{n}\dot{\boldsymbol{a}} + \frac{\Delta t^2}{2}\,{}^{n}\ddot{\boldsymbol{a}}, \tag{15}$$

$${}^{n+1}\dot{\boldsymbol{a}} = {}^{n}\dot{\boldsymbol{a}} + \frac{\Delta t}{2}({}^{n}\ddot{\boldsymbol{a}} + {}^{n+1}\ddot{\boldsymbol{a}}), \tag{16}$$

where Δt is the time step size. Here the nodal values at the current time step n are known, and with some reformulations, it is possible to obtain the expression

$$ {}^{n}\ddot{\boldsymbol{a}} = \frac{1}{\Delta t^2}({}^{n+1}\boldsymbol{a} - 2\,{}^{n}\boldsymbol{a} + {}^{n-1}\boldsymbol{a}), \tag{17} $$

see [21] for full derivation. Using (17) in (14) gives the expression

$$ {}^{n+1}\boldsymbol{a} = 2\,{}^{n}\boldsymbol{a} - {}^{n-1}\boldsymbol{a} + \boldsymbol{M}^{-1}\Delta t^2({}^{n}\boldsymbol{f}^{ext} - \boldsymbol{f}^{int}({}^{n}\boldsymbol{a})), \tag{18} $$

and here the nodal values on the right-hand side are known and the internal forces can be resolved. This expression can solve dynamic problems directly without any iterations and is further enhanced if the mass matrix $\boldsymbol{M}$ is lumped, meaning it is a diagonal matrix, then its inversion is trivial and gives the solution without solving any equation system. However, the downside of this simplification is that the explicit solution is only conditionally stable. There exists a critical time step, which if exceeded will result in solutions that are unstable with errors that grow rapidly. In LS-DYNA this critical time step is generally defined as the time it takes for a shock wave to travel through the smallest element as [22]

$$ \Delta t = \frac{L}{c}, \tag{19} $$

where L is the length of the element and c is the wave speed which for solids is defined as

$$ c_{so} = \sqrt{\frac{E}{\rho(1-\nu^2)}}, \tag{20} $$

and for shells as

$$ c_{sh} = \sqrt{\frac{E(1-\nu)}{(1+\nu)(1-2\nu)\rho}}, \tag{21} $$

where E is Young's modulus, ρ is the density, and ν is Poisson's ratio. LS-DYNA makes sure that the critical time step is not exceeded by regulating the density of the elements (using so-called mass scaling) if needed and by so doing decreases the size of c, which in turn increases the size of the critical time step.

2.4 Material Failure Model CrachFEM

CrachFEM [18] is a material failure model made by MATFEM that describes the behaviour of materials in explicit FE-codes. It can be used for shell and solid element

models in commercial explicit FE-codes such as LS-DYNA, Abaqus, Radioss, and PAM-Crash/Stamp [22]. There are three types of material failure in CrachFEM; ductile normal fracture, ductile shear fracture, and instability. These three fracture types are visualized in Fig. 2.9. Shell elements use all three criteria, while solid elements only use the ductile normal/shear fracture criteria.

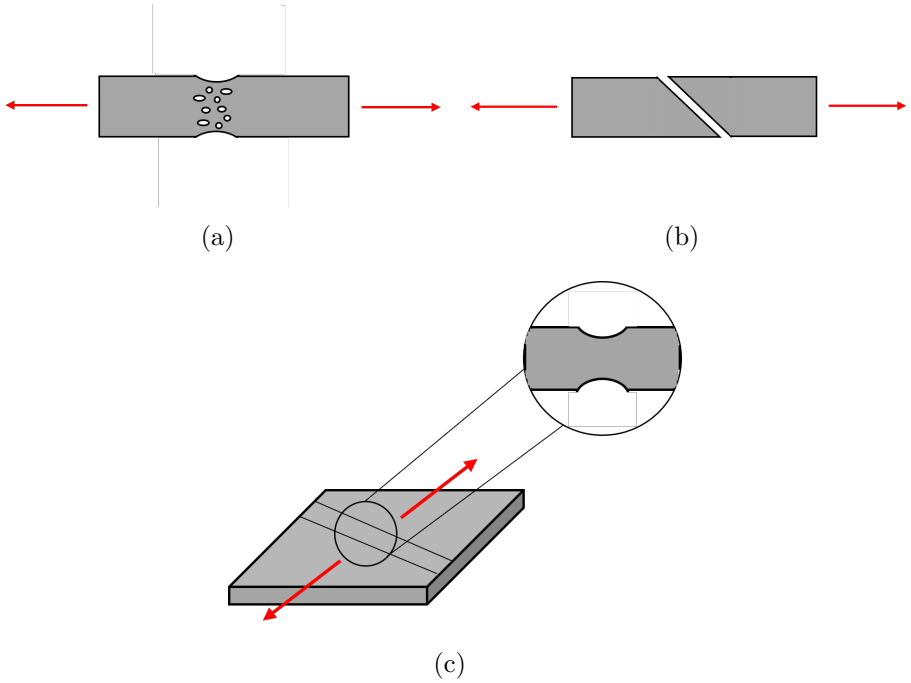

Figure 2.9: CrachFEM fracture types; (a) ductile normal fracture, (b) ductile shear fracture, (c) instability. Inspired by [18].

CrachFEM accumulates fracture risk until the probability of fracture reaches a unity value. The fracture risk is defined as [18]

$$\psi = \frac{\varepsilon_{eq}}{\varepsilon_{eq,f}}, \tag{22}$$

where ε_{eq} is the equivalent plastic strain, and $\varepsilon_{eq,f}$ is the failure strain. It should be mentioned that all three CrachFEM failure criteria follow this failure logic.

2.4.1 Ductile Normal Fracture

Using the plane stress assumption, the failure strain $\varepsilon_{eq,f}$ can be modeled as a function of triaxiality η. CrachFEM scales the triaxiality value with a factor of 3 compared to the parameter formulation used in (6), and the expression used for plane stress is formulated as

$$\eta_{cf} = \frac{3\sigma_h}{\sigma_{eq}} = \frac{\sigma_1 + \sigma_2}{\sqrt{\sigma_1^2 - \sigma_1\sigma_2 + \sigma_2^2}}, \tag{23}$$

where σ_1 and σ_2 are the two principal stresses used in plane stress.

This 2D stress state works well when using shell elements, but when solid elements are used the triaxiality parameter alone is not enough to describe a 3D stress state since the values are not unique. The failure strain model is therefore extended to be dependent on two parameters. In CrachFEM the second parameter introduced is the normalized major stress, which relates the first principal stress σ_1 to the von Mises stress σ_{eq} as

$$\bar{\sigma}_1 = \frac{\sigma_1}{\sigma_{eq}} \quad . \tag{24}$$

The extended model for the failure strain is called the beta-model, and the material-dependent stress state parameter β is calculated as

$$\beta = \beta(\bar{\sigma}_1, \eta_{cf}) = \frac{1 - s\eta_{cf}}{\bar{\sigma}_1}, \tag{25}$$

and the failure strain is calculated as

$$\varepsilon_{eq,f} = d \cdot e^{q\beta}, \tag{26}$$

where s, d, and q are material parameters [18].

It is common to use the LAP when visualizing the failure surfaces. Using the relation between the normalized major stress and the LAP as [9]

$$\sigma_1 = \left(\eta + \frac{2}{3}\cos\theta\right)\sigma_{eq}, \tag{27}$$

then (25) can be rewritten using (11) to give the expression

$$\beta = \frac{1 - s \cdot \eta_{cf}}{\frac{\eta_{cf}}{3} + \frac{2}{3}\cos\left((1-\bar{\theta})(\frac{\pi}{6})\right)}. \tag{28}$$

2.4.2 Ductile Shear Fracture

Following the same logic as in the ductile normal fracture model, the ductile shear fracture model is represented as a function of the shear stress parameter θ_m, where θ_m is calculated as

$$\theta_m = \theta_m(\tau_{max}, \eta_{cf}) = \frac{1 - k_{SF} \cdot \eta_{cf}}{w}, \tag{29}$$

and w is the ratio of maximum shear stress to the von Mises stress and is calculated as

$$w = \frac{\tau_{max}}{\sigma_{eq}}. \tag{30}$$

Also, τ_{max} is calculated as

$$\tau_{max} = \frac{\sigma_1 - \sigma_3}{2}, \tag{31}$$

where σ_1 and σ_3 are the maximum and the minimum principal stresses respectively and the failure strain $\varepsilon_{eq,f}$ is calculated as

$$\varepsilon_{eq,f} = \frac{\varepsilon_{NF}^{+} \cdot \sinh(f \cdot (\theta - \theta^{-})) + \varepsilon_{NF}^{-} \cdot \sinh(f \cdot (\theta - \theta^{+}))}{\sinh(f \cdot (\theta^{-} - \theta^{+}))}, \tag{32}$$

where θ^{+} and θ^{-} are calculated as

$$\begin{aligned} \theta^{+} &= 2 \cdot (1 - 2 \cdot k_{SF}), \\ \theta^{-} &= 2 \cdot (1 + 2 \cdot k_{SF}), \end{aligned} \tag{33}$$

where ε_{NF}^{+}, ε_{NF}^{-}, f, and k_{SF} are material parameters [18].

Usually, the ductile shear fracture models are visualized on a 3D surface, where the third parameter could be the LAP $\bar{\theta}$. Thereby, the previous model could be re-written as a function of η_{cf} and $\bar{\theta}$, where σ_3 is re-written as [9]

$$\sigma_3 = \left[\eta + \frac{2}{3}\cos(\frac{2}{3}\pi - \theta)\right]\sigma_{eq}, \tag{34}$$

and it is expressed in terms of LAP $\bar{\theta}$ using (11) by combining (30), (31), and (34). The parameter w is expressed as

$$w = \frac{\left[\frac{\eta_{cf}}{3} + \frac{2}{3}\cos\left(\frac{\pi}{6}(1-\bar{\theta})\right)\right] - \left[\frac{\eta_{cf}}{3} + \frac{2}{3}\cos\left(\frac{4\pi}{3} - \frac{\pi}{6}(1-\bar{\theta})\right)\right]}{2}, \tag{35}$$

and by combining (29) and (35), θ_m is expressed as

$$\theta_m = \frac{2(1 - k_{SF} \cdot \eta_{cf})}{\left[\frac{\eta_{cf}}{3} + \frac{2}{3}\cos\left(\frac{\pi}{6}(1-\bar{\theta})\right)\right] - \left[\frac{\eta_{cf}}{3} + \frac{2}{3}\cos\left(\frac{\pi}{6}(8-(1-\bar{\theta}))\right)\right]}. \tag{36}$$

2.4.3 Instability Fracture

The instability failure is more tricky to define than ductile normal/shear failure. Still, some define it as failure induced by local thinning in the surface occurring during the tensile test. Others define it as failure induced by diffused necking through the cross-section, as seen in Fig. 2.10.

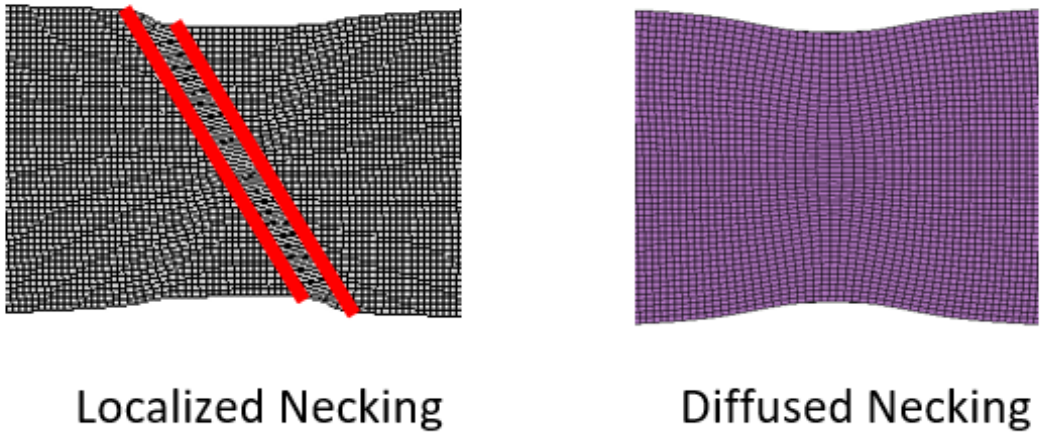

Figure 2.10: Difference between localized and diffused necking.

CrachFEM only adopts instability failure for shell elements, while suggesting both an exact and an approximate instability calculation. Unfortunately, the exact solution consumes a lot of simulation time, so the approximate solution is adopted. The approximate calculation is implemented for low plastic strain and if there is a possibility of instability risk, the exact solution is adopted. The instability risk approximation is defined as

$$\Psi_{FLC} = \frac{\varepsilon_{eq}}{\varepsilon_{eq}^{FLC}(\alpha)}, \tag{37}$$

where ε_{eq} is the von Mises equivalent strain, which is calculated as

$$d\varepsilon_{eq} = \frac{2}{\sqrt{3}} \cdot \sqrt{d\varepsilon_1^2 + d\varepsilon_1 d\varepsilon_2 + d\varepsilon_2^2}\,. \tag{38}$$

The principle strain ratio α is defined as

$$\alpha = \frac{d\varepsilon_2}{d\varepsilon_1}, \tag{39}$$

and $\varepsilon_{eq}^{FLC}(\alpha)$ is defined as

$$\varepsilon_{eq}^{FLC} = \begin{cases} \dfrac{\varepsilon_{(0)} \cdot \sqrt{1 + k_1 \cdot \alpha + (k_1 \cdot \alpha)^2}}{1 + k_1 \cdot \alpha} & \text{for } \alpha \leq 0 \\ \varepsilon_{(0)} + \left(k_2 - \varepsilon_{(0)}\right) \cdot \alpha^{3/2} + \left(\varepsilon_{(1)-k_2} \cdot \alpha^2\right) & \text{for } \alpha > 0 \ , \end{cases} \tag{40}$$

where $\varepsilon_{(0)}$, $\varepsilon_{(1)}$, k_1, and k_2 are material parameters [18].

Equation (40) specifically addresses instability, pinpointing the localized necking point failure. However, beyond this stage, where the physical fracture occurs, denoted by a red X-mark in Fig. 2.10, there exists a set of equations with ambiguity. Notably, these equations are not outlined in the CrachFEM manual. This instability calculation covers what CrachFEM terms as post-instability criteria.

It should be mentioned that α and η have a relation shown in Table II [23]

TABLE II
TRIAXIALITY AND PRINCIPLE STRAIN RATIO RELATION

Load case	η	α
Biaxial tension	2/3	1
Plane strain tension	$1/\sqrt{3}$	0
Uniaxial tension	1/3	-1/2
Pure shear	0	-1
Uniaxial compression	-1/3	-2
Plane strain compression	$-1/\sqrt{3}$	$-\infty$
Biaxial compression	-2/3	1

and this relation is governed by the curve shown in Fig. 2.11.

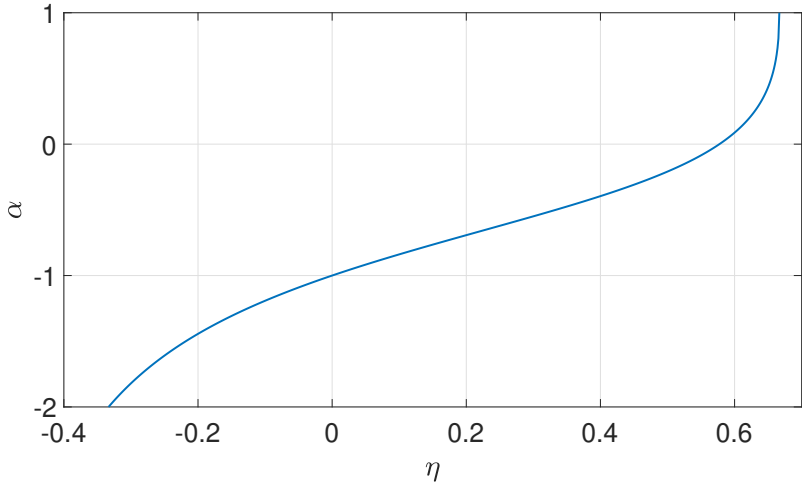

Figure 2.11: Triaxiality η and principle strain ratio α equivalency.

The previous curve shown in Fig. 2.11 is governed by the formula

$$\alpha = \frac{-\eta}{6\eta^2 - 2} \cdot (-3\eta + \sqrt{12 - 27\eta^2}) - 1. \tag{41}$$

2.5 Lode Dependent Instability

Swift [17] determined the condition for forming a diffused necking is satisfied when the load reaches the maximum along all principal directions [24]

$$\begin{aligned} \dot{\sigma}_1 &= \sigma_1 \dot{e}_1 \\ \dot{\sigma}_2 &= \sigma_2 \dot{e}_2 \\ \dot{\sigma}_3 &= \sigma_3 \dot{e}_3, \end{aligned} \tag{42}$$

where e is the plastic strain increment. The rate of change in the yield function can be defined as

$$\dot{\sigma}_{eq} = \frac{\partial \sigma_{eq}}{\partial \sigma_1}\dot{\sigma}_1 + \frac{\partial \sigma_{eq}}{\partial \sigma_2}\dot{\sigma}_2 + \frac{\partial \sigma_{eq}}{\partial \sigma_3}\dot{\sigma}_3 = \frac{d\sigma_{eq}}{d\varepsilon_{eq}}\dot{\varepsilon}_{eq} \tag{43}$$

and plastic strain increment e also derived from a flow rule

$$\dot{e}_i = \dot{\varepsilon}_{eq}\frac{\partial \sigma_p}{\partial \sigma_i}, \tag{44}$$

where the plastic potential σ_p is conventionally equivalent to the yield surface function

$$\sigma_p = \sigma_{eq}(\sigma_1, \sigma_2, \sigma_3) \ . \tag{45}$$

By assuming the von Mises yield function in (7) and the Swift hardening law in (13), and combining (42), (43), and (44) results in the expression

$$\dot{\sigma}_{eq} = \left(\frac{\partial \sigma_{eq}}{\partial \sigma_1}\right)^2 \sigma_1 \dot{\varepsilon}_{eq} + \left(\frac{\partial \sigma_{eq}}{\partial \sigma_2}\right)^2 \sigma_2 \dot{\varepsilon}_{eq} + \left(\frac{\partial \sigma_{eq}}{\partial \sigma_3}\right)^2 \sigma_3 \dot{\varepsilon}_{eq} = \frac{d\sigma_{eq}}{d\varepsilon_{eq}}\dot{\varepsilon}_{eq} \ . \tag{46}$$

This gives

$$\frac{d\sigma_{eq}}{d\varepsilon_{eq}} = \left(\frac{\partial \sigma_{eq}}{\partial \sigma_1}\right)^2 \sigma_1 + \left(\frac{\partial \sigma_{eq}}{\partial \sigma_2}\right)^2 \sigma_2 + \left(\frac{\partial \sigma_{eq}}{\partial \sigma_3}\right)^2 \sigma_3 \tag{47}$$

and from (47) and (7)

$$\begin{aligned} \frac{d\sigma_{eq}}{d\varepsilon_{eq}} &= \left(\frac{\partial \sigma_{eq}}{\partial \sigma_1}\right)^2 \sigma_1 + \left(\frac{\partial \sigma_{eq}}{\partial \sigma_2}\right)^2 \sigma_2 + \left(\frac{\partial \sigma_{eq}}{\partial \sigma_3}\right)^2 \sigma_3 \\ &= \frac{1}{2}(3\eta + \cos(3\theta))\sigma_{eq}. \end{aligned} \tag{48}$$

By comparing this to $d\sigma_{eq}/d\varepsilon_{eq}$ of Swift hardening (13) as

$$\frac{1}{2}(3\eta + \cos(3\theta))K(\varepsilon_0 + \varepsilon_{eq})^n = Kn(\varepsilon_0 + \varepsilon_{eq})^{n-1}, \tag{49}$$

which gives the strain-based instability criteria for a von Mises material

$$\varepsilon_{eq,f} = \frac{2n}{3\eta + \cos(3\theta)} - \varepsilon_0. \tag{50}$$

Given that $\theta = \arccos(\xi)/3$, this gives

$$\varepsilon_{eq,f} = \frac{2n}{3\eta + \xi} - \varepsilon_0. \tag{51}$$

2.6 Cockcroft-Latham

The ductile fracture usually occurs at maximum tensile stress. Cockcroft-Latham [9] suggested a model as a function of maximum principal stress as in (52)

$$\int_0^{\varepsilon_{eq,f}} \sigma_1 \, d\varepsilon_{eq} = C_1, \tag{52}$$

where C_1 is a material constant. This relation could further down be presented in terms of LAP and triaxiality using (27) as

$$\int_0^{\varepsilon_{eq,f}} \left[\eta + \frac{2}{3}\cos\left(\frac{\pi}{6}(1-\bar{\theta})\right)\right] K(\varepsilon_0 + \varepsilon_{eq})^n \, d\varepsilon_{eq} = C_1, \tag{53}$$

where $\sigma_{eq} = K(\varepsilon_0 + \varepsilon_{eq})^n$ is the Swift hardening law, K is a strength coefficient, ε_{eq} is the equivalent plastic strain, and n is a hardening exponent that varies for different materials, and ε_0 is a strain shift parameter. (53) expresses the Cockcroft-Latham model in the space of $(\eta, \bar{\theta}, \varepsilon_{eq})$, and the failure strain $\varepsilon_{eq,f}$ could be expressed explicitly by

$$\varepsilon_{eq,f} = \left[\varepsilon_0^{n+1} + \frac{C_1(n+1)}{K\left[\eta + \frac{2}{3}\cos\left(\frac{\pi}{6}(1-\bar{\theta})\right)\right]}\right]^{\frac{1}{n+1}} - \varepsilon_0 \tag{54}$$

2.7 Modified Mohr-Coulomb

The Mohr-Coulomb criterion, widely used for brittle materials, was modified [7] to predict the ductile fracture behavior of metals like aluminium. The MMC [9] is explicitly expressed as

$$\varepsilon_{eq,f} = \left\{ \left[\frac{K}{C_{10}}\left(C_{11} + \frac{\sqrt{3}}{2-\sqrt{3}}(1-C_{11})\left[\sec\left(\frac{\pi\bar{\theta}}{6}\right) - 1\right]\right)\right] \times \left[\sqrt{\frac{1+C_9^2}{3}}\cos\left(\frac{\pi\bar{\theta}}{6}\right) + C_9\left[\eta + \frac{1}{3}\sin\left(\frac{\pi\bar{\theta}}{6}\right)\right]\right] \right\}^{-1/n}. \tag{55}$$

Where C_9, C_{10}, and C_{11} are material constants.

2.8 GISSMO

GISSMO (Generalized Incremental Stress State Model) is a damage model that takes the incremental information about the damage D into account [19]. D is valued between $0 \leq D \leq 1$, and the value 1 means a fully damaged specimen. The damage incremental formula is

$$\Delta D = \frac{n D^{1-\frac{1}{n}}}{\varepsilon_f} \Delta \varepsilon_p, \tag{56}$$

where n is the damage exponent, ε_f is the failure strain, and ε_p is the plastic strain and D is evaluated as

$$D = \left(\frac{\varepsilon_p}{\varepsilon_f} \right)^n. \tag{57}$$

In the context of GISSMO, the instability measure F ranges from 0 to 1, where $F = 0$ indicates complete material stability and $F = 1$ signifies maximum instability or damage. As F progresses from 0 to 1, it represents the increasing damage within the material. When F reaches 1, it triggers the coupling of damage to the stress response, indicating that the material's damage has reached a critical point, significantly affecting its ability to withstand stress. In simulations, monitoring F helps track the damage progression, and reaching $F = 1$ marks a critical change in the material's behavior, indicating a severely reduced capacity to handle stress and potential failure. The instability F is also an incremental value, with the instability incremental formula as

$$\Delta F = \frac{n F^{1-\frac{1}{n}}}{\varepsilon_{p,loc}} \Delta \varepsilon_p, \tag{58}$$

where $\varepsilon_{p,loc}$ is the equivalent plastic strain to instability. When the instability F reaches a unity, the damage reaches a critical value D_{crit}, and by knowing this value, the true stress tensor can be evaluated by

$$\sigma_{true} = \sigma_{eff} \left[1 - \left(\frac{D - D_{crit}}{1 - D_{crit}} \right)^m \right], \tag{59}$$

where σ_{eff} is the effective stress and m is the fade exponent which is calibrated to match experimental data.

The GISSMO model is just a damage model that must be complemented by another plasticity model, which is an essential difference between CrachFEM and GISSMO.

The beta and theta models could also be implemented in GISSMO as well as other models such as Cockcroft-Latham and MMC criterion. GISSMO also has the capability of adopting instability failure curves for both solids (if instability is extended for 3D solid elements) and shells, which is an advantage over the CrachFEM model.

Another crucial point to note is that both the CrachFEM failure model and the GISSMO damage model are driven by plastic strain, meaning that fracture is dictated by the plastic strain. In contrast, other failure or damage criteria utilize alternative methods, such as energy-based models.

3

Methods

This chapter outlines the detailed steps taken to complete the assessment of the plane stress model. Figures have had their y-axis values removed for the company's confidentiality.

3.1 Hardening Curve Effect

Before examining the impact of any failure model, it is essential to first analyze the hardening curve without any failures included. This preliminary step helps to understand how various components of the FE solver influence the results. To achieve this, it is necessary to isolate all other factors, including the normal failure curve, shear failure curve, and instability failure curve. The analysis is conducted using a medium-sized mesh with a 1 mm mesh size and different solid element types, as well as a fine-sized mesh with a 0.2 mm mesh size and different solid element types. Additionally, a second-order study is performed to assess the impact of having more nodes in the tetrahedral elements. Second-order hexahedral elements are excluded from the analysis due to significant issues encountered within the solver.

3.2 CrachFEM

Understanding how the material failure model works was a crucial part of being able to evaluate its performance. The analysis was conducted with models of varying complexity, starting with the simplest model of single elements of both shells and solids.

3.2.1 Single Element Simulation

Two rows of seven elements were made, as shown in Fig. 3.1 following the same load cases shown in Fig. 2.3.

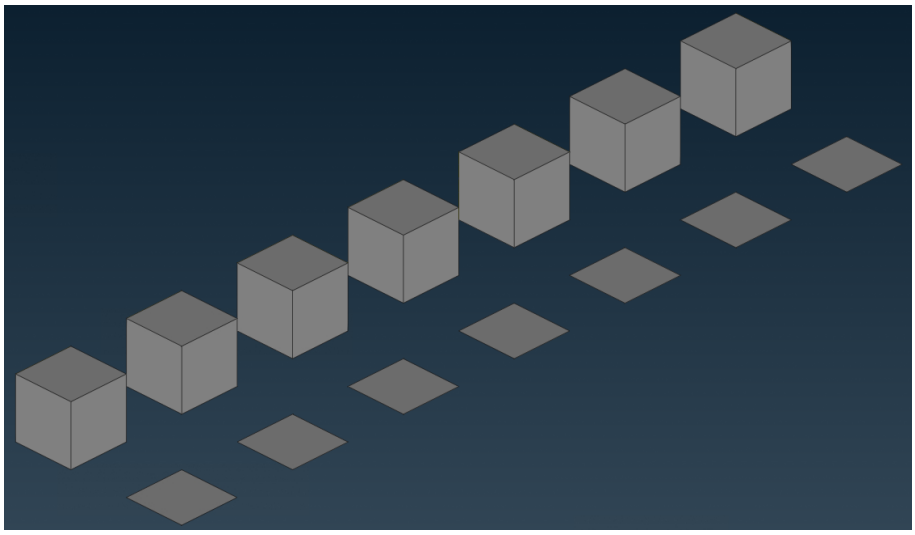

Figure 3.1: The single elements used in the simulation. The load cases used from left to right are biaxial compression, plane strain compression, uniaxial compression, pure shear, uniaxial tension, plane strain tension, and biaxial tension.

Using these load cases for different values of triaxiality, the fracture points could be mapped to the material-specific failure criteria curves, since each element was subjected to a constant value of triaxiality. For the solid elements, only the ductile normal and ductile shear failure criteria were active, while shells also used the instability criterion. For the instability criterion, the simulation was run with the post-instability criterion both on and off.

To capture the theoretical values as closely as possible, the plastic orthotropic parameter was deactivated to ensure a von Mises yield locus was used. Additionally, the parameters shifting the normal fracture curve were deactivated.

For this project, both fracture anisotropic material cards and transverse isotropy fracture material cards were tested in the single element simulation. However, only the transverse isotropy was continued, as some components of the fracture anisotropic material cards were dysfunctional for unknown reasons.

3.2.2 Coupons in Tension

With an understanding of how the basic model behaved, the analysis could move on to the next step. This included the simulation of several coupon models used in physical experiments for different loading cases. In the tensile coupon tests, different mesh sizes, element types, and element orders were used to find a configuration for solid elements that would yield results that were closest to the shell elements. This configuration would later be used in the other coupon tests. The purpose of doing the virtual coupon testing was to compare them to the physical test specimens that the failure curves for the extruded aluminium were calibrated with. The model was calibrated for the use of shell elements, so it was important to verify how the shells matched the physical tests and how solid elements with different element types and

order behaved in comparison.

The first step for the coupon test was to create a digital model that used the same dimensions as the physical test. The schematic for the coupons in tension are shown in Fig. 3.2, Fig. 3.3, and Fig. 3.4.

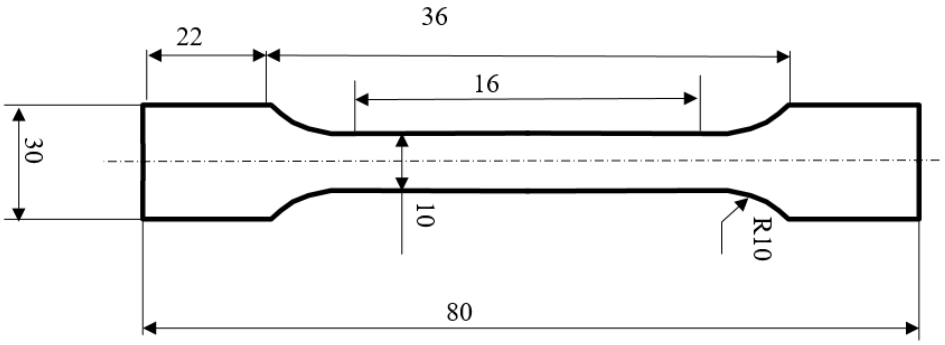

Figure 3.2: Schematic of the coupon used in tensile test, where the thickness is 2 mm.

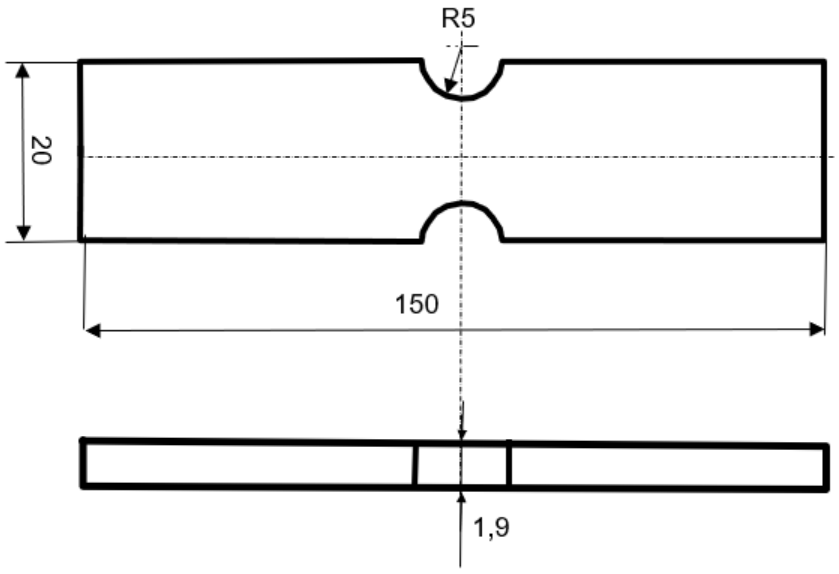

Figure 3.3: Schematic of the waisted coupon used in the tensile test.

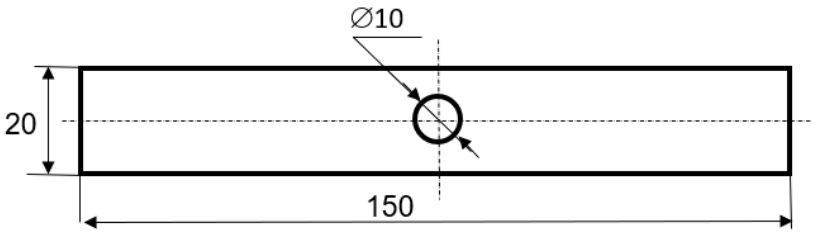

Figure 3.4: Schematic of the coupon with a hole used in the tensile test, where the thickness is 1.95 mm.

When the model in Fig. 3.2 was made, a set of configurations were used to be able to see how the type of elements and mesh size affect the results. The configuration that gave the closest match between solids and shells, and the physical test would later be reused in the other coupon tests. The different mesh sizes were coarse, medium, and fine, with element lengths 3, 1, and 0.2 mm respectively. In addition to different mesh sizes, different element formulations of solid elements were tested, and only one type of shell element was used. The used elements were first-order quadrilateral elements for shells. First-order hexahedral elements and tetrahedral elements, as well as second-order tetrahedral elements were used for solid elements. Different configurations were tested as well. The tensile coupon was tested with post-instability criterion both active and inactive.

The post-processing was then done to visualize the section force which was measured at several cross-sections through the coupon. The LAP as a function of triaxiality, and equivalent plastic strain as a function of triaxiality were visualized as well. These measurements were taken for the critical element, meaning the first element to fail in the coupon. This post-processing step would later be repeated for other coupons.

The LS-DYNA simulation was made to mimic the real test which was fixed on the left side of the coupon and pulled on the right side through rigid links attached to beam elements as seen in Fig. 3.5, Fig. 3.6, and Fig. 3.7. The right side of the coupon was fixed in all degrees of freedom except the elongation in positive x-direction. The elongation was measured between two nodes distanced 7.5 mm right and left from the middle of the coupon.

There were some slight differences in boundary conditions between the different kind of coupons. The coupon showed in Fig. 3.2 had fixed boundary conditions in displacement and rotation 22 mm from the left side and fixed boundary conditions in displacement and rotation expect the elongation in x-direction 22 mm from the right side. While the coupon in Fig. 3.3 covered 55 mm from both sides and hole

coupon covered 30 mm from both sides.

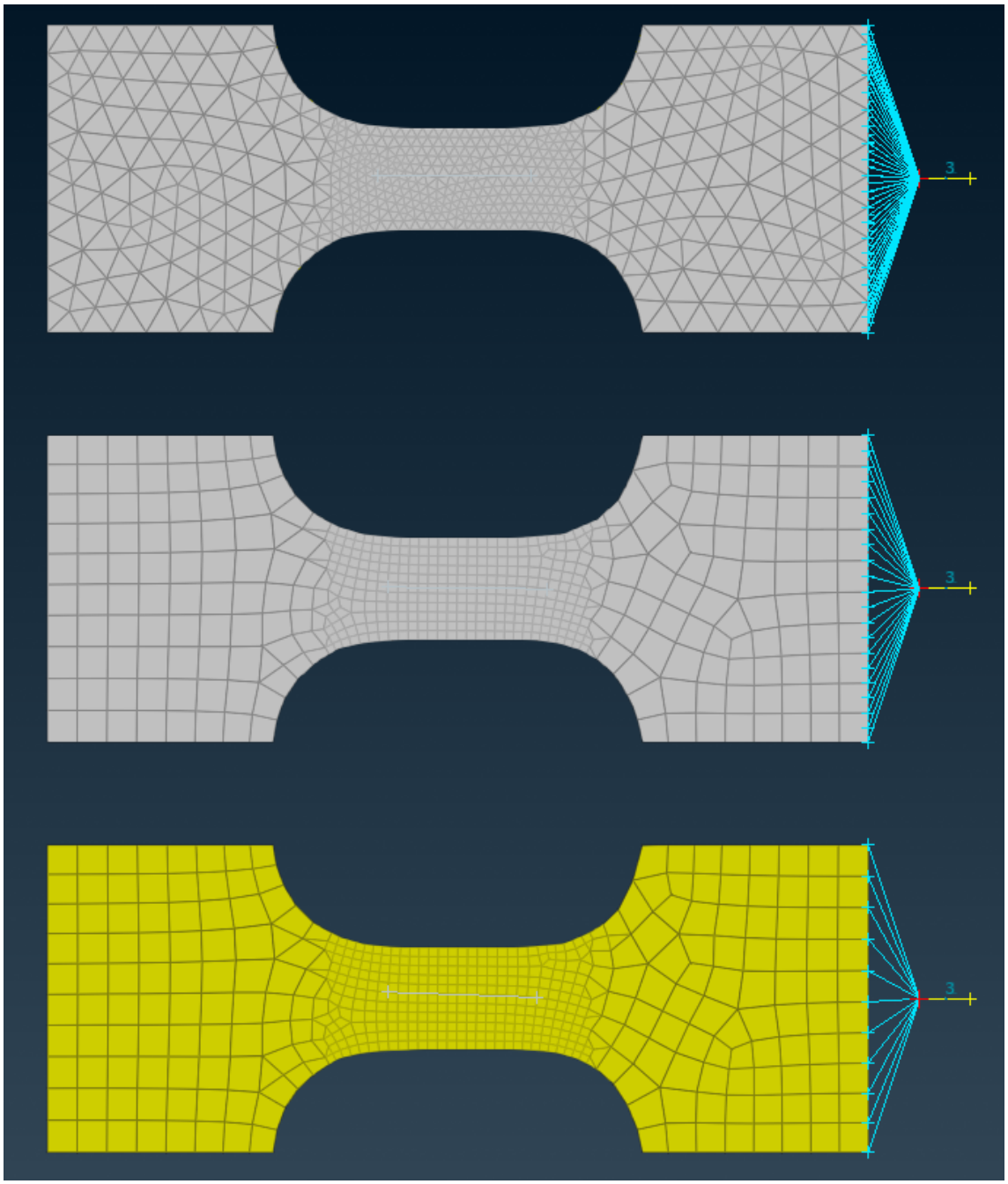

Figure 3.5: LS-DYNA simulation settings, where the lower coupon is quadrilateral shell elements, the middle one is hexahedral elements and the upper one is tetrahedral elements. The element size is 3 mm at the side and 1 mm in the middle.

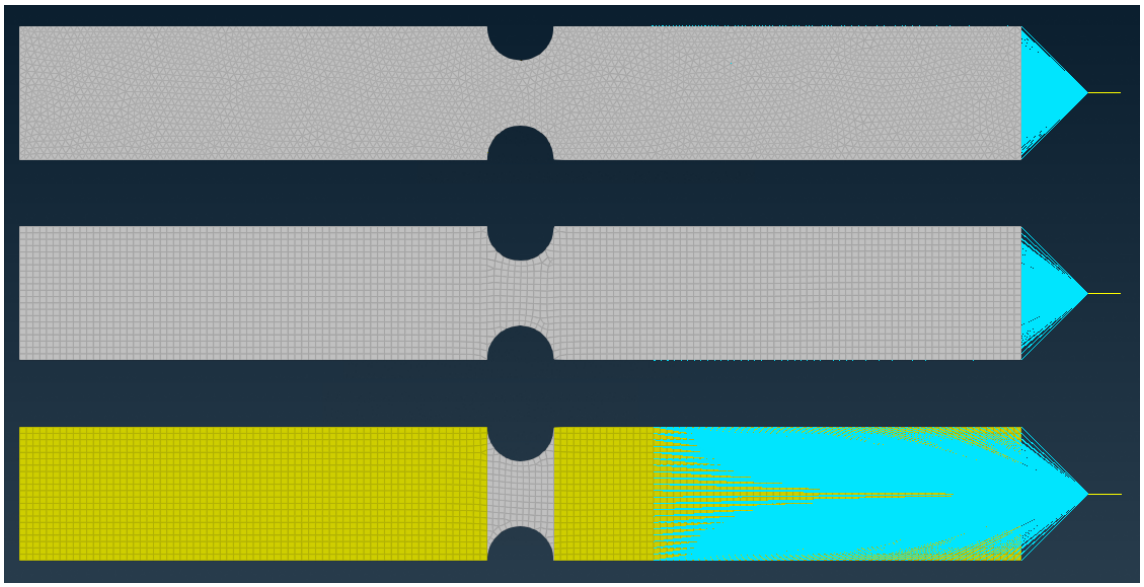

Figure 3.6: LS-DYNA simulation settings for waisted coupon, where the lower coupon is quadrilateral shell elements, the middle one is hexahedral elements and the upper one is tetrahedral elements. The element size is 1 mm.

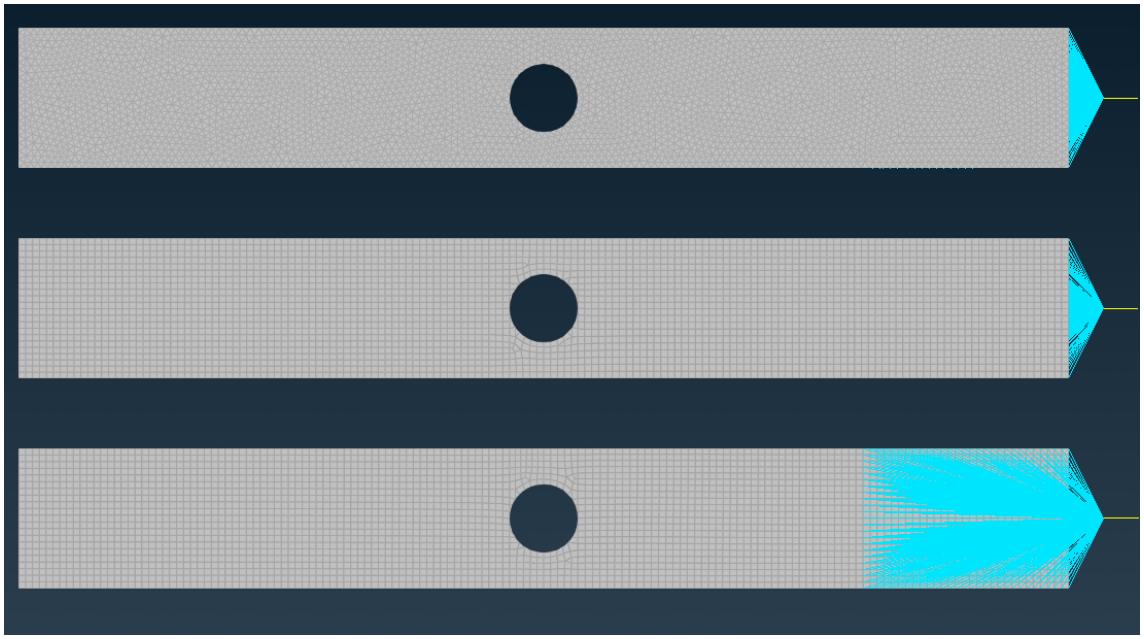

Figure 3.7: LS-DYNA simulation settings for the hole coupon, where the lower coupon is quadrilateral shell elements, the middle one is hexahedral elements and the upper one is tetrahedral elements. The element size is 1 mm.

3.3 GISSMO

In order to validate the CrachFEM results, the GISSMO damage model was also used. This model implemented properties that CrachFEM does not, such as incorporating instability failure for 3D solid elements and regularization.

3.3.1 Sanity Check

Before introducing instability considerations for 3D solid elements and utilizing GISSMO's additional functionalities, the beta and theta failure models were integrated into the GISSMO damage cards while considering that GISSMO could only accommodate one failure curve. In this scenario the critical failure curve, derived from both shear and normal failure curves, was adapted, as shown in Fig. 3.8. A comparison was then made between the results obtained from GISSMO and those from CrachFEM, with instability disabled in the latter. The purpose of disabling instability in CrachFEM was to isolate the failure criteria to only include the ductile normal/shear fracture curves since the instability criterion was not present for 3D solid elements.

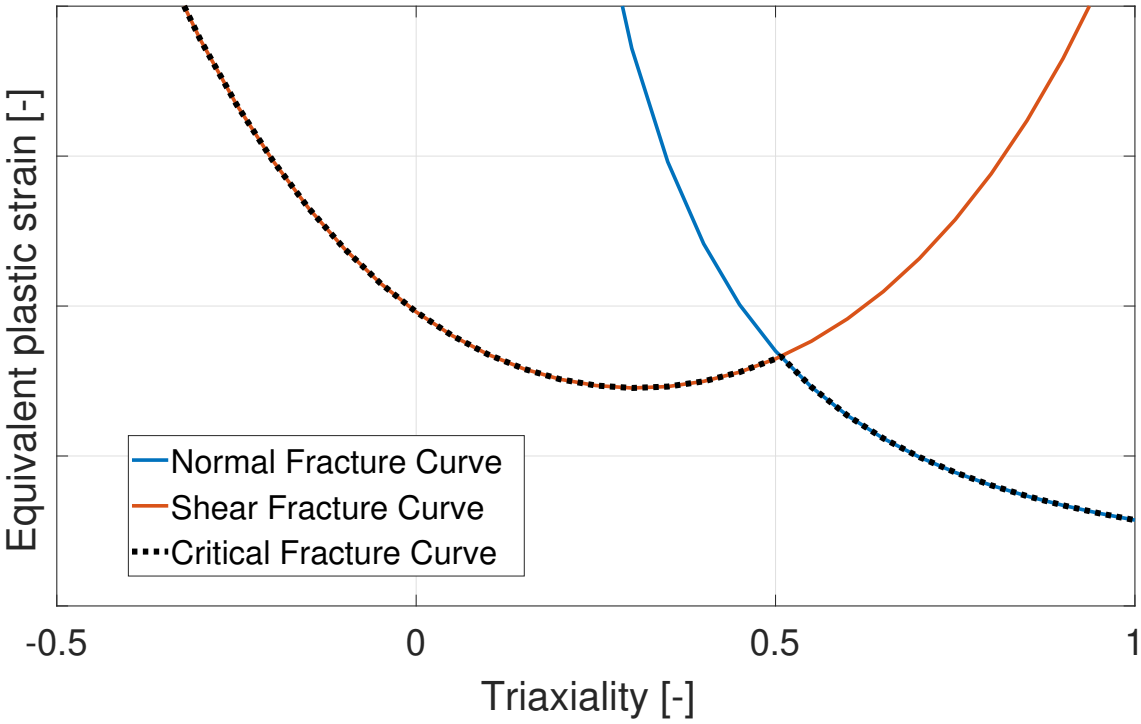

Figure 3.8: The critical failure curve considered in GISSMO.

3.3.2 Plastic Anisotropy with GISSMO

This step extended the sanity check by examining the differences in the plastic anisotropy model in CrachFEM when compared to the Barlat plastic anisotropy model. It was important to determine whether there was a significant difference between the optimized model using Barlat and the built-in model within CrachFEM.

3.3.3 Regularization

In GISSMO there exist a function that allows for automatic value scaling depending on mesh size to reduce the difference in results between different mesh densities. To use this function, a table was constructed by using a very fine mesh as a reference and giving it a parameter value of 1. In this case a mesh density of 0.2 mm was used as a reference, and the table was constructed by comparing the mesh densities 0.5 mm, 1 mm, and 3 mm to the reference. In Fig. 3.9 an example of the differences in values between the mesh densities can be seen. Here the curves are fitted to the reference by using the DYNAmore program LS-OPT. After regularization the curves are shifted to closely match the reference as can be seen in Fig. 3.10.

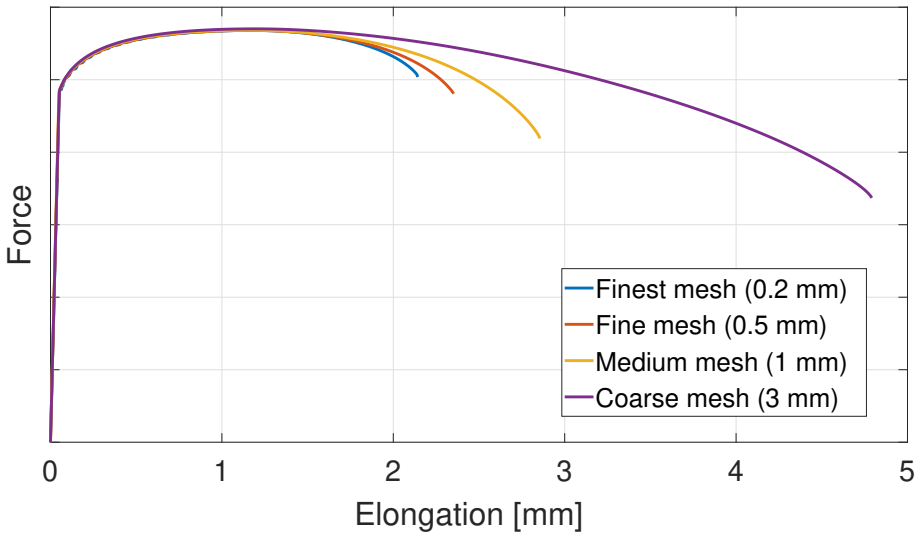

Figure 3.9: An example of curves of different mesh densities in a tension test. Here the regularization will scale the curves to match the 0.2 mm reference.

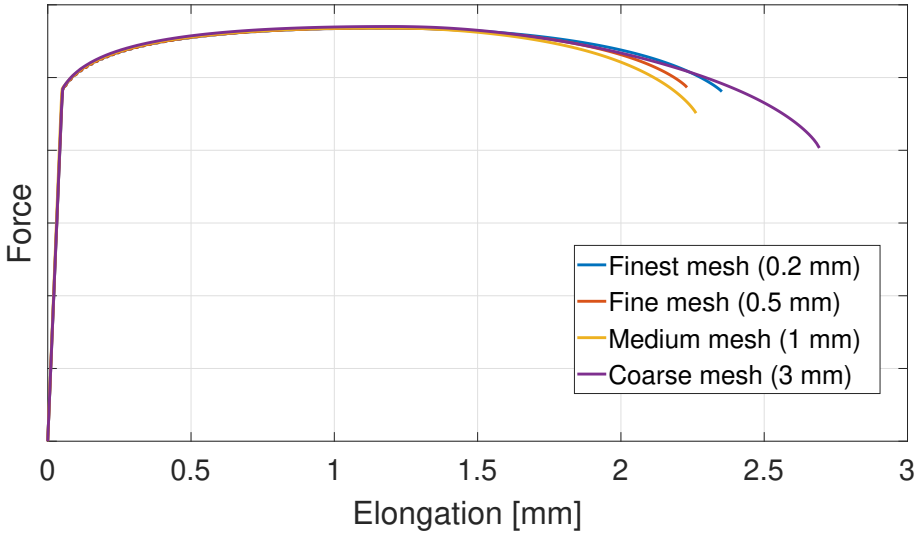

Figure 3.10: Curves of different mesh densities in a tension test after being shifted by regularization.

3.3.4 Incorporating Instability for 3D Solids & Studying the Effect of Damage and Fade Exponents

The instability in the CrachFEM failure model was limited to a 2D-representation, defined by a single curve of equivalent plastic strain versus triaxiality. Therefore, this failure curve was not used in GISSMO. Instead, GISSMO incorporated the Lode-dependent instability discussed in Section 2.5. This approach was further compared to CrachFEM shells, which were previously validated against test data. In other words, the extension of instability to be Lode-dependent was made to allow GISSMO to add instability to 3D solid elements. It was not possible to define a failure surface directly in GISSMO, multiple equivalent plastic stress versus triaxiality curves had to be defined for a number of LAP values between the upper and lower bounds. These curves together spanned a surface in which GISSMO could interpolate values from. Following this implementation, the effect of the damage exponent n and the fade exponent m could be investigated.

3.3.5 Cockcroft-Latham & Modified Mohr-Coulomb Using GISSMO

Another feasible alternative to using CrachFEM was to construct a failure curve based on existing criteria from the literature. One such criterion was the Cockcroft-Latham model, and another was the MCC criterion, both re-expressed in terms of the LAP and triaxiality as shown in (54) and (55). LS-DYNA had already included a corresponding material model for Cockcroft-Latham called MAT258 which the model incorporated in GISSMO was compared to as shown in Fig. 3.11. However, no such model existed for the MCC and so its implementation was carefully reviewed and debugged. This involved ensuring an accurate representation of its parameters in terms of LAP and triaxiality, and thorough validation against theoretical predic-

tions and experimental data to confirm its reliability. It must be mentioned that Cockcroft-Latham material parameter C_1 in (54) is calibrated from tensile coupon experimentation while MMC material parameters C_9, C_{10}, and C_{11} in (55) are calibrated from failure plastic strain based on CrachFEM's beta/theta model. Both calibrated failure surfaces are shown in Fig. 3.12 and Fig. 3.13.

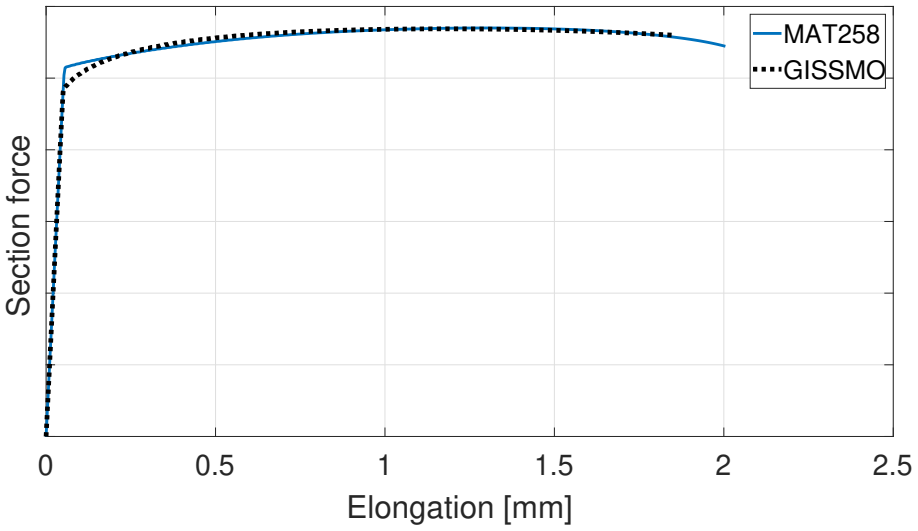

Figure 3.11: Cockcroft-Latham in GISSMO versus MAT258.

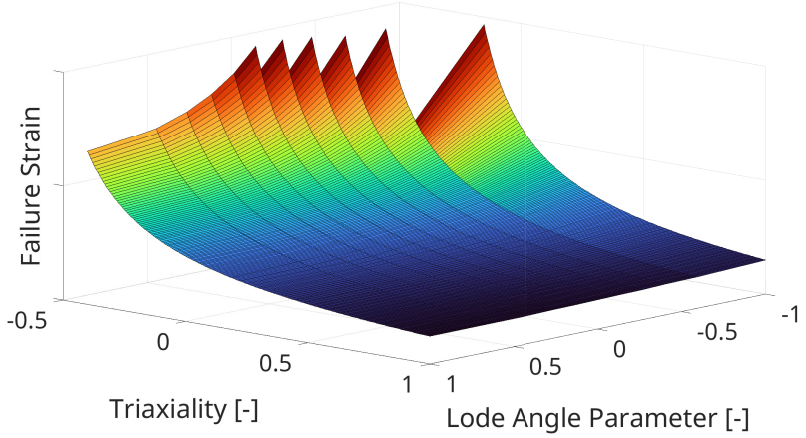

Figure 3.12: Cockcroft-Latham failure surface. The surface is generally flat along the LAP axis.

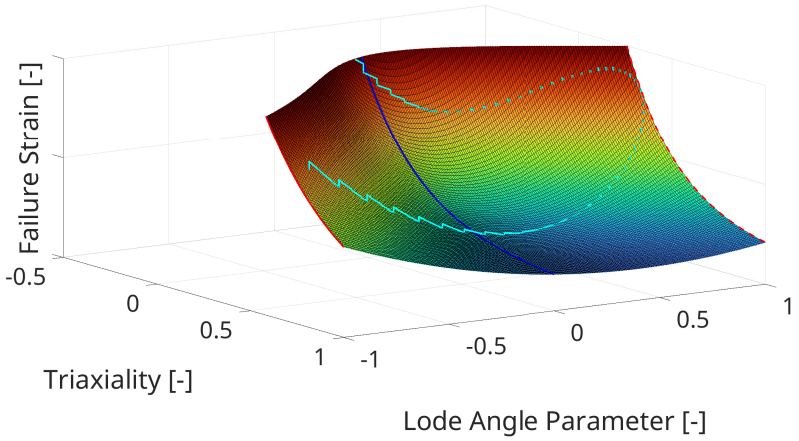

Figure 3.13: MMC failure surface. The surface is varying along both triaxiality and LAP axes.

3.4 Component Simulation

As a final step in the analysis, a component used in physical three-point-bending tests was simulated. Already made digital models were available and a visualisation of the component with a groove in the middle can be seen in Fig. 3.14.

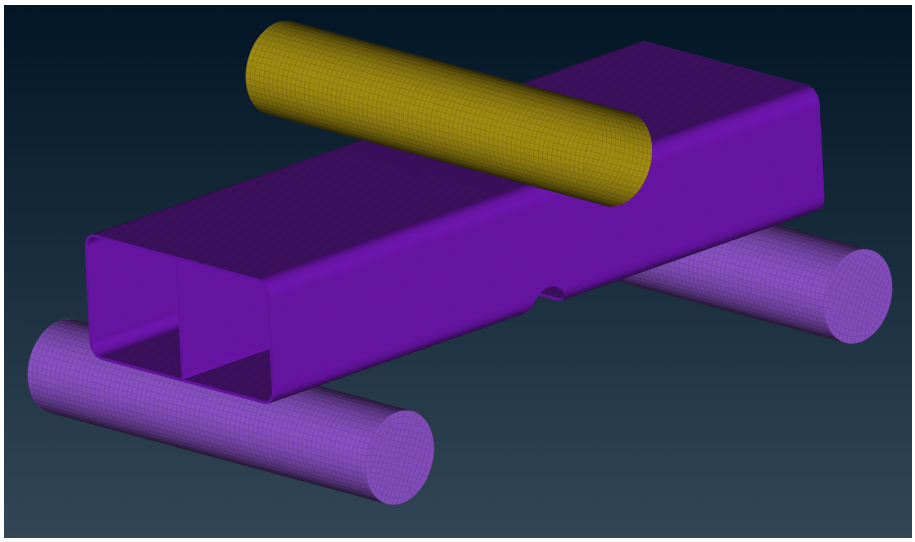

Figure 3.14: LS-DYNA simulation model for the component testing in three-point-bending with a groove in the center.

The simulations were done using the best configurations for solid 3D elements in both CrachFEM and GISSMO, where the latter model was also reran using the Cockcroft-Latham and MMC failure criteria. Three different mesh densities were used for hexahedral elements, while only two were used for the tetrahedral elements. The models were evaluated by comparing the results to experimental data.

4

Results & Discussion

In this chapter all the results of following the methods used for the assessment of the plane stress model are presented and discussed. Figures have had their y-axis values removed for the company's confidentiality.

4.1 Hardening Curve Effect

From the simulations without any failure criteria active, the shell elements are shown to have a softening effect due to the constraint that they have to follow the plane stress conditions, demonstrated by Fig. 4.1. This shows that already on the plastic level without any failure present, solids and shells behave differently. Since failure in the models is plastic strain based, differences in shells and solids for plastic strain evolution are expected. The second-order tetrahedrons with a 1 mm mesh size exhibit behavior that falls between the curves for the 1 mm mesh and the 0.2 mm mesh, indicating the impact of additional nodes in the elements. One observation to be made is that explicit simulations are more sensitive to time-stepping.

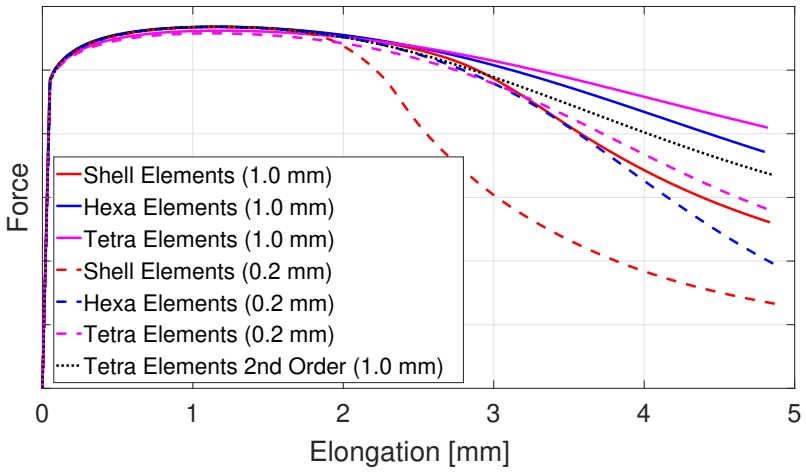

Figure 4.1: Evolution of the plastic strains without any failure criteria active for tensile coupon tests with various mesh sizes and element types.

Both Fig. 4.2 and Fig. 4.3 highlight the discrepancies between the medium mesh and the fine mesh in capturing necking. Both mesh sizes can capture different stages of necking even without the failure curve. However, only the fine shell mesh accurately

captures both diffused and localized necking, as shown in the zoomed-in section of Fig. 4.3. Due to the geometrical characteristics of the solid elements and out-of-plane strain, both solid and shell elements exhibit a reduction in thickness.

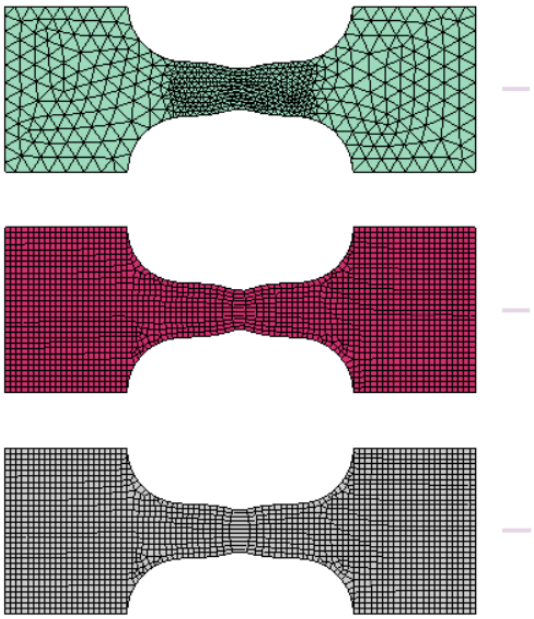

Figure 4.2: Visualization of plastic deformations and diffused necking without any failure criteria active for medium mesh (1.0 mm).

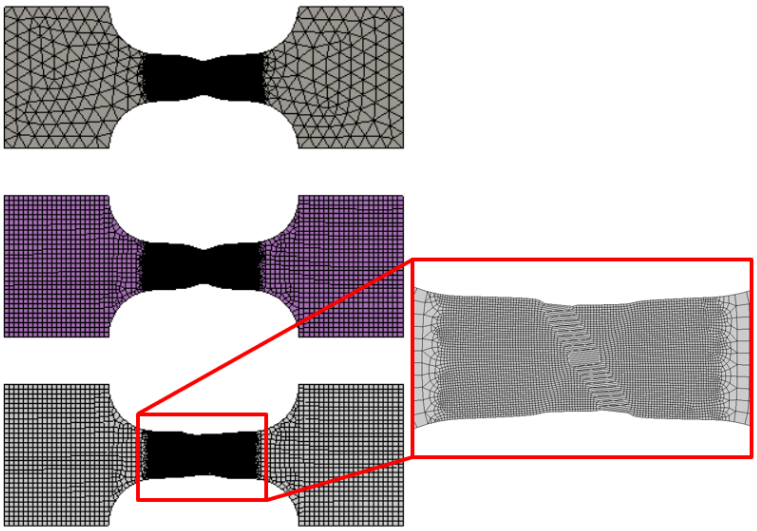

Figure 4.3: Visualization of plastic deformations and necking without any failure criteria active for fine mesh (0.2 mm). The zoomed in area shows localized necking.

The instability failure curve appears to induce failure due to necking, but it does not generate the necking itself. The purpose of introducing instability failure was not to capture necking in the shell elements, but rather to capture the failure induced by necking. This necking effect is something that solid elements capture geometrically. The results indicate that both shell and solid element formulations can capture this type of failure.

Although Fig. 2.5 indicates that analytically, the coupon must undergo both diffused and localized necking before failure, this does not guarantee that the FE-solver will capture these phenomena. In fact, it appears that solid elements will never accurately capture localized necking.

4.2 CrachFEM

This section covers the analysis made in the material failure model model CrachFEM with different coupon simulations.

4.2.1 Single Element Simulation

The single element simulations were expected to behave in accordance with theoretical predictions. The solid elements failed either at the normal fracture curve or the shear fracture curve, while the shell elements failed precisely on the instability fracture curve when the post-instability criterion was disabled. What the instability curve represents is the initial instability curve. The post-instability induced by localized necking could not be modeled due to insufficient information on its governing mechanisms.

The difference between Fig. 4.4 and Fig. 4.5 lies in their fracture behavior. Fig. 4.4 considers anisotropic fracture, whereas Fig. 4.5 considers transversely isotropic fracture. Due to the lack of reliable information about the beta and theta parameters in the anisotropic fracture failure material cards, the remainder of the project will proceed using the transversely isotropic material fracture cards.

The purpose of the single-element simulation was to understand and verify that the CrachFEM material model function as expected. Specifically, it aimed to ensure that solid and shell elements fail at the correct positions on their respective curves; the instability curve for shells and the shear and normal ductile failure curves for solids. Additionally, all of these elements have the same theoretical triaxiality values, as shown in Fig. 2.3. The reason the elements fail on the theoretical points of the failure curve is due to the constant strain evolution path.

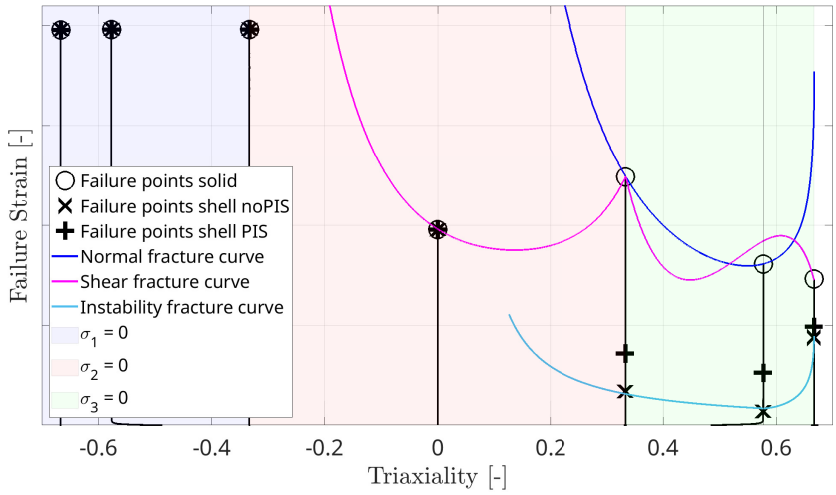

Figure 4.4: Evolution of triaxiality and points of failure for single elements in CrachFEM. The failure curves used is for anisotropic aluminium in a quasi-static condition.

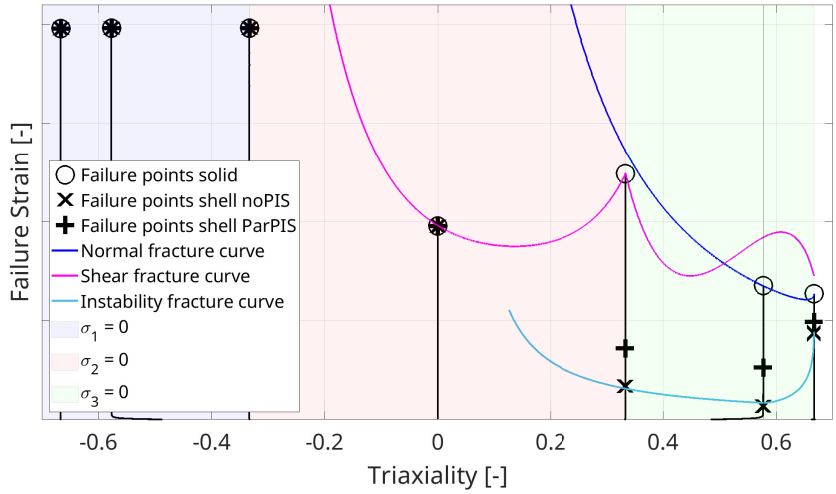

Figure 4.5: Evolution of triaxiality and points of failure for single elements in CrachFEM. The failure curves used is for transversal isotropic aluminium in a quasi-static condition.

4.2.2 Coupons in Tension

As shown in Fig. 4.6, the section forces exhibit discrepancies between the experimental data and all simulated data using both shell and solid elements. This mismatch might be attributed to potential errors in measuring the thickness. If the thickness was slightly reduced, the amplitude of the CrachFEM simulated data might align more closely with the experimental data. However, all CrachFEM solid elements with various mesh sizes and types, as well as shell elements (except those with a fine

0.2 mm mesh size), show discrepancies in elongation values.

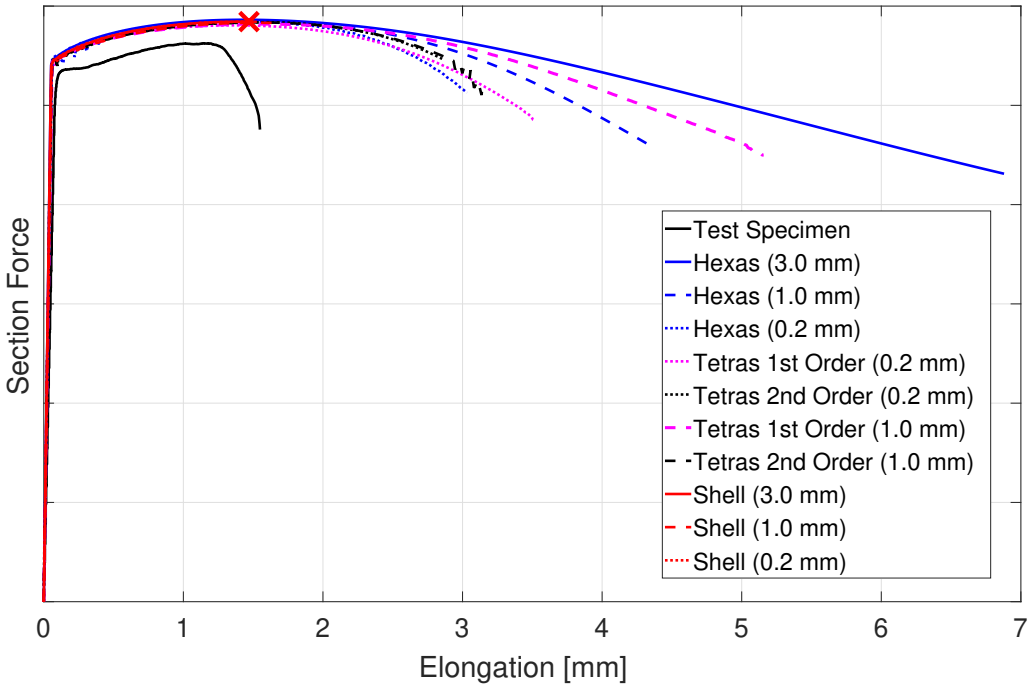

Figure 4.6: Evolution of section forces with respect to elongation in CrachFEM for all configurations of tensile coupons compared to the experimental test specimens. The X-marker shows the point of failure for the Shell (0.2 mm) coupon.

The only mesh size that matches the experimental curves in terms of elongation value was the 0.2 mm mesh shell elements, the point of fracture is indicated by the cross marker in Fig. 4.6. This suggests that regardless of the mesh size used for solid elements they do not match the experimental curves. It requires a highly dense mesh for the shell elements to replicate the experimental results accurately. This was expected since the current experimental data were used to calibrate the shell element model in CrachFEM. In order to align the elongation levels of shell elements with that of the experimental curves, the post-instability phase had to be disabled.

Fig. 4.7(b), Fig. 4.8(b), and Fig. 4.9(b) illustrate the development of LAP across various element types in response to triaxiality. Here it is shown that the shells follow the plane stress curve, and solid elements deviates toward higher triaxialities and reaches values up to 0.7. By checking the LAP value at the point of failure and plotting the respective failure curve, Fig. 4.7(a), Fig. 4.8(a), and Fig. 4.9(a) illustrate the development of plastic strain across various element types in response to triaxiality, which show that that shell elements fail almost at the initial instability failure curve. Solid elements are inconsistent regarding the failure point, and it does not seem to have a standard typical shift value of overshooting above the curve for different element sizes and types. Contrary to the strain path evolution for single elements shown in Fig. 4.4 and Fig. 4.5, the path is non-linear. This is why the point of failure is not exactly on the failure curve and instead happens before

or after reaching the curve. The CrachFEM failure model accumulates damage according to how far the plastic strain curve is from the failure curve. This is the reason for the overshooting above the failure curve. One remedy to this would be shifting the failure curves downwards by scaling the fracture strain values with a parameter value, causing the damage to accumulate faster at the same strain levels. This would in turn lead to more predictive failure, and eventually, the plastic strain evolution would result in an on-curve failure. But an option of shifting the failure curve downwards was not available in CrachFEM.

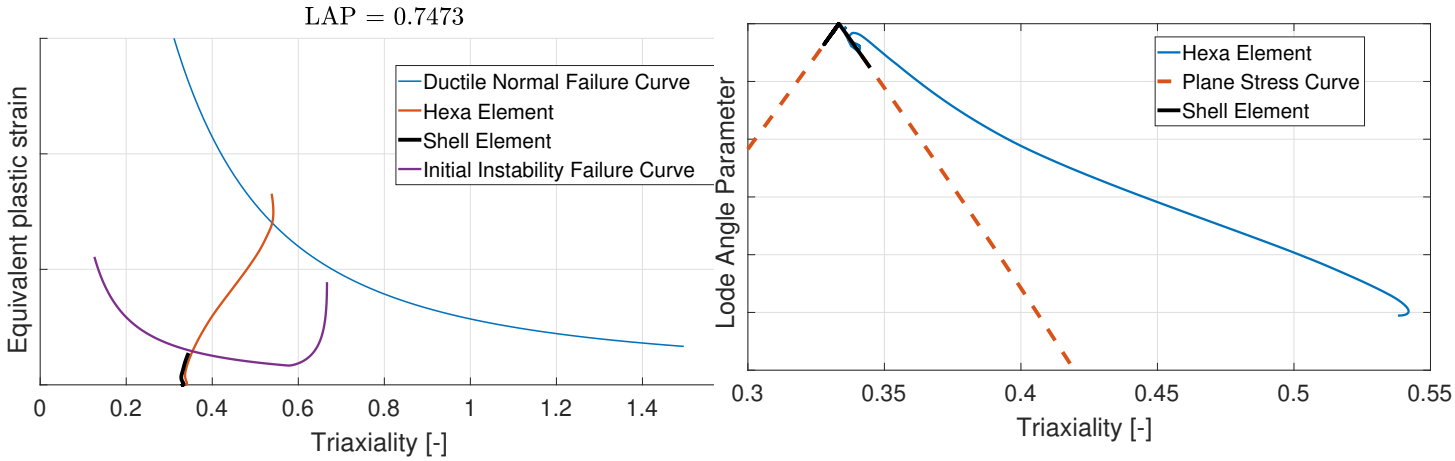

(a) Evolution of equivalent plastic strain with respect to triaxiality for tensile coarse (3 mm) coupon. Both the critical shell and hexa elements are plotted with their respective failure curve.

(b) Evolution of LAP with respect to triaxiality for tensile coarse (3 mm) coupon in CrachFEM. The critical shell and hexa elements are plotted together with the plane stress curve.

Figure 4.7: Evolution of equivalent plastic strain vs. triaxiality, and evolution of LAP vs. triaxiality for tensile coarse (3 mm) coupon.

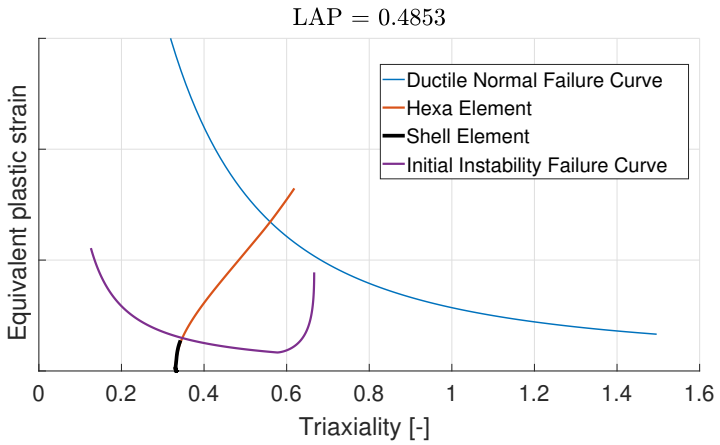

(a) Evolution of equivalent plastic strain with respect to triaxiality for tensile medium (1 mm) coupon in CrachFEM. Both the critical shell and hexa elements are plotted with their respective failure curve.

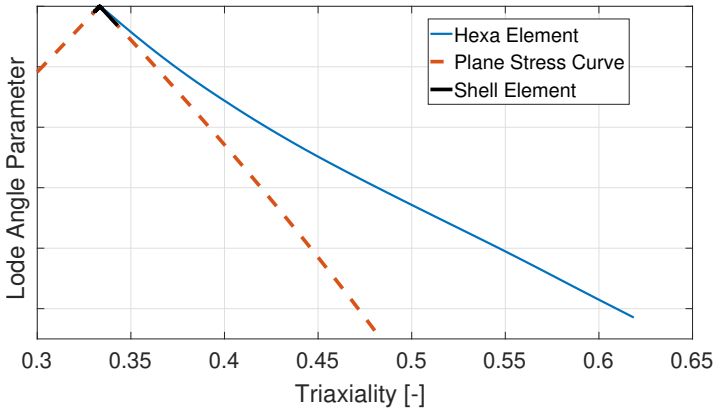

(b) Evolution of LAP with respect to triaxiality for tensile medium (1 mm) coupon in CrachFEM. The critical shell and hexa elements are plotted together with the plane stress curve.

Figure 4.8: Evolution of equivalent plastic strain vs. triaxiality, and evolution of LAP vs. triaxiality for tensile medium (1 mm) coupon.

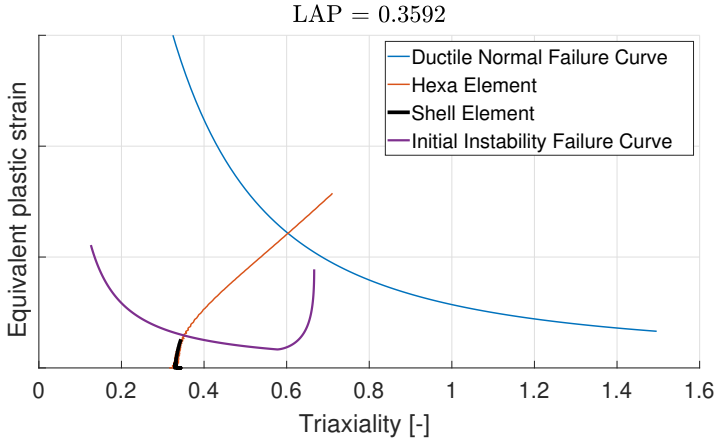

(a) Evolution of equivalent plastic strain with respect to triaxiality for tensile fine (0.2 mm) coupon in CrachFEM. Both the critical shell and hexa elements are plotted with their respective failure curve.

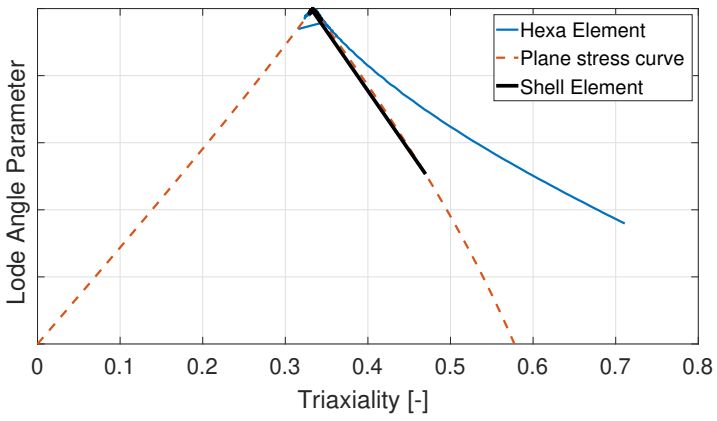

(b) Evolution of LAP with respect to triaxiality for tensile fine (0.2 mm) coupon in CrachFEM. The critical shell and hexa elements are plotted together with the plane stress curve.

Figure 4.9: Evolution of equivalent plastic strain vs. triaxiality, and evolution of LAP vs. triaxiality for tensile fine (0.2 mm) coupon.

The tetra elements shown in Fig 4.10(a) and Fig 4.10(b) are also failing after the failure curve. When compared to the previous hexa elements, these tetra elements demonstrate a slightly greater shift post-failure. Notably, the second-order tetra elements exhibit even more significant deviation from the failure curve and deviate from the theoretical triaxiality value of 1/3. This deviation trends towards higher triaxiality, raising questions about the reliability and accuracy of tetra elements in representing the actual behavior under these conditions.

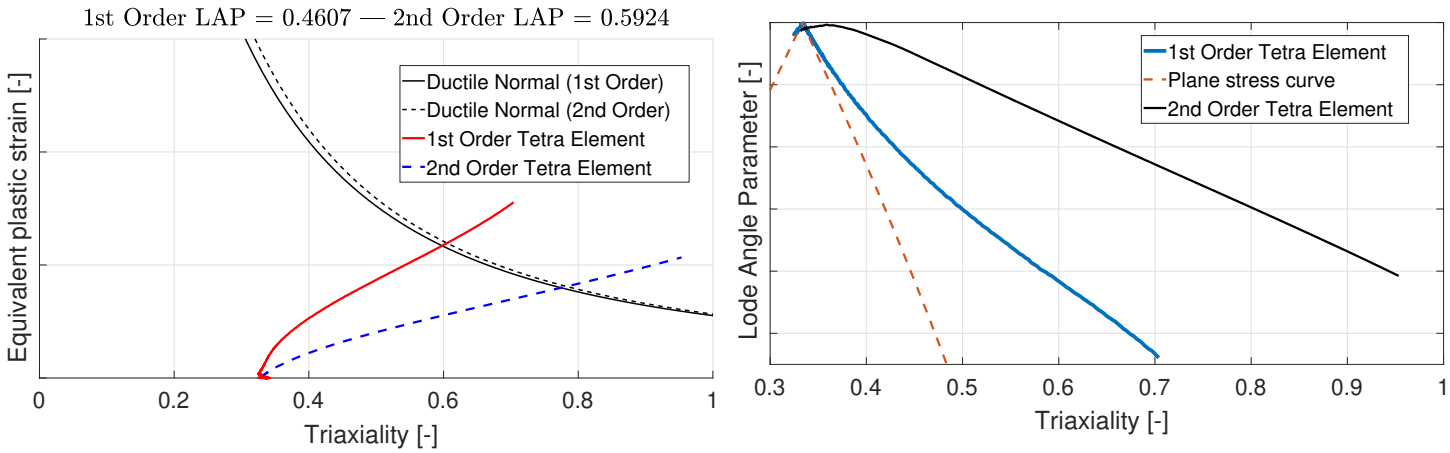

(a) Evolution of equivalent plastic strain with respect to triaxiality for tensile fine (0.2 mm) coupon in CrachFEM. Both the critical 1st order tetra and 2nd order tetra elements are plotted with their respective failure curve.

(b) Evolution of LAP with respect to triaxiality for tensile fine (0.2 mm) coupon in CrachFEM. The critical 1st order tetra and 2nd order tetra elements are plotted together with the plane stress curve.

Figure 4.10: Evolution of equivalent plastic strain vs. triaxiality, and evolution of LAP vs. triaxiality for tensile fine (0.2 mm) coupon using both 1st and 2nd order tetra elements.

The waisted coupon in tension exhibits an even greater discrepancy among all simulated element types, shown in Fig. 4.11. The shell elements soften more than the experimental curves, though they do show some matching in elongation level. In contrast, the solid elements do not match the experimental results in either force amplitude or elongation level, raising questions about the validity of the beta and theta failure model for solid elements.

Fig. 4.12(a) shows the deviation from the plane stress curve for hexa elements, while the tetra elements behave randomly, raising questions about the accuracy and reliability of tetra elements and whether they are a good choice for different loading conditions. Both Fig. 4.13(a) and Fig. 4.13(b) emphasize that tetra elements behave completely randomly. Hexa elements show an overshoot after the failure curve, similar to the tensile coupon, which might be attributed to the stress-strain path after localized instability until the fracture point. However, the premature failure of tetra elements before the curve completes is entirely nonphysical. Fig. 4.12(b) shows a significant overshoot in the plastic strain development beyond the initial instability curve since the post-instability phase is activated. This inconsistency highlights another downside of the CrachFEM failure model, as there are discrepancies in the simulation settings for different coupons.

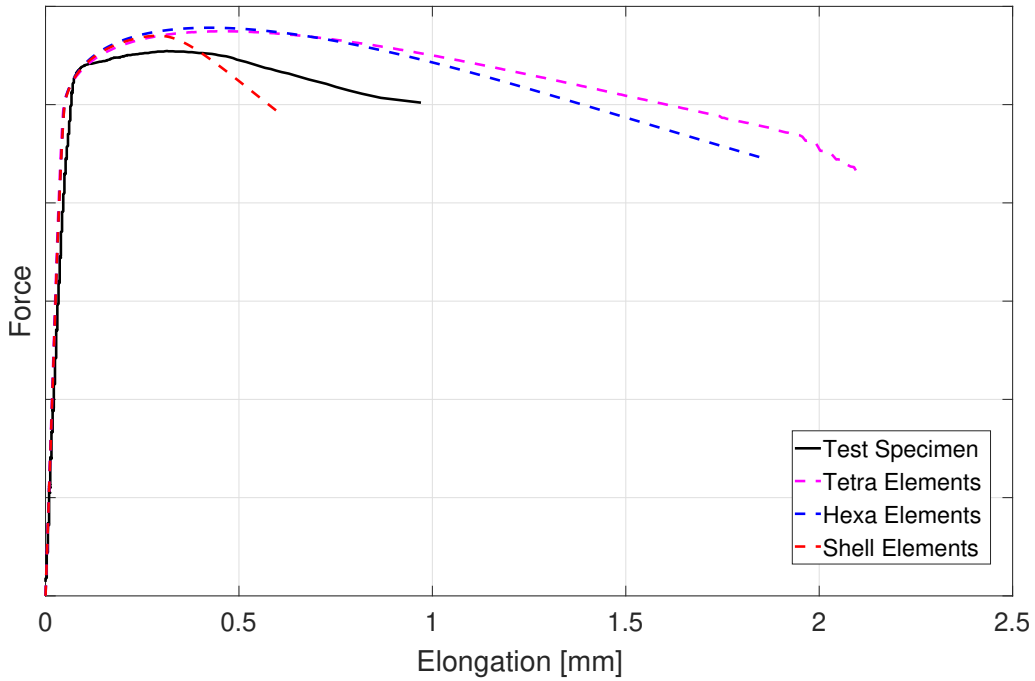

Figure 4.11: Evolution of the section forces with respect to the elongation for medium mesh (1 mm) waist coupon in CrachFEM. The different types of elements are compared to the experimental test specimens.

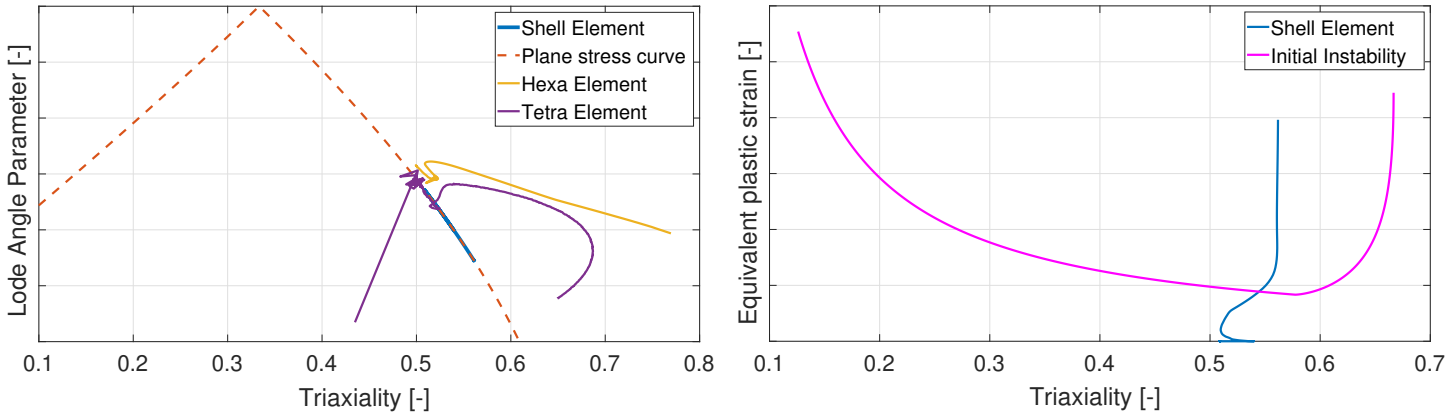

(a) Evolution of LAP with respect to triaxiality for waist medium (1 mm) coupon in CrachFEM. The critical shell, hexa, and tetra elements are plotted together with the plane stress curve.

(b) Evolution of equivalent plastic strain with respect to triaxiality for waist medium (1 mm) coupon in CrachFEM. The critical shell element is plotted together with the initial instability curve.

Figure 4.12: Evolution of LAP vs. triaxiality, and evolution of equivalent plastic strain vs. triaxiality for the critical shell element for waist medium (1 mm) coupon.

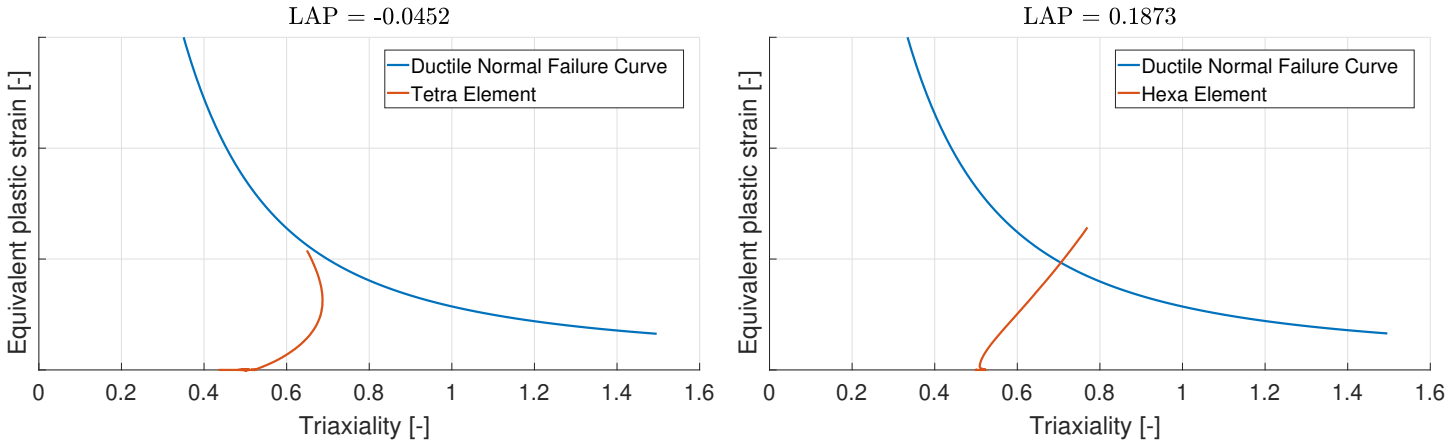

(a) Evolution of equivalent plastic strain with respect to triaxiality for waist medium (1 mm) coupon in CrachFEM. The critical tetra element is plotted together with its failure curve.

(b) Evolution of equivalent plastic strain with respect to triaxiality for waist medium (1 mm) coupon in CrachFEM. The critical hexa element is plotted together with its failure curve.

Figure 4.13: Evolution of equivalent plastic strain vs. triaxiality for the critical tetra and hexa elements for waist medium (1 mm) coupon.

The hole coupon section forces in Fig. 4.14 demonstrate similar conclusions to those of the waist coupon. However, the shell elements show better matching to experimental results in terms of both force amplitude and elongation level. Conversely, the solid elements continue to mismatch with the experimental results.

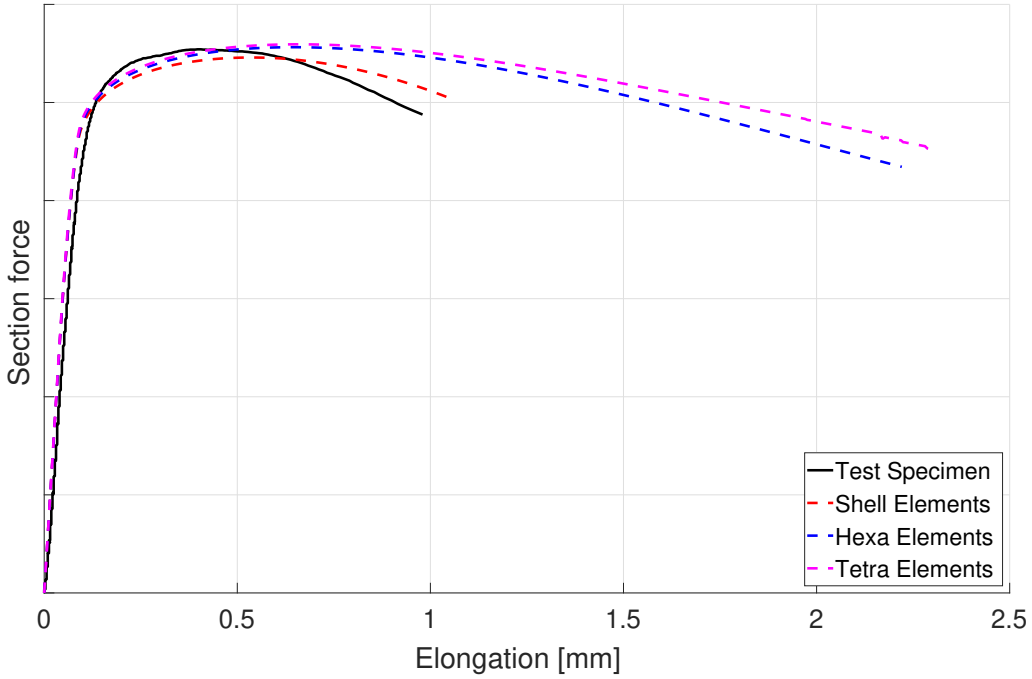

Figure 4.14: Evolution of the section forces with respect to the elongation for medium (1 mm) mesh hole coupon in CrachFEM. The different types of elements are compared to the experimental test specimens.

Regarding the triaxiality and LAP in Fig. 4.15(a), both hexa and tetra elements behave randomly. This randomness is evident in Fig. 4.16(a) and Fig. 4.16(b), which show nonphysical plastic strain development with triaxiality. This inconsistency highlights the failure of the CrachFEM model to behave reasonably. Additionally, there is a discrepancy between different coupon simulations when using the same simulation settings, as seen in Fig. 4.15(b), which illustrates the application of post-instability failure criteria.

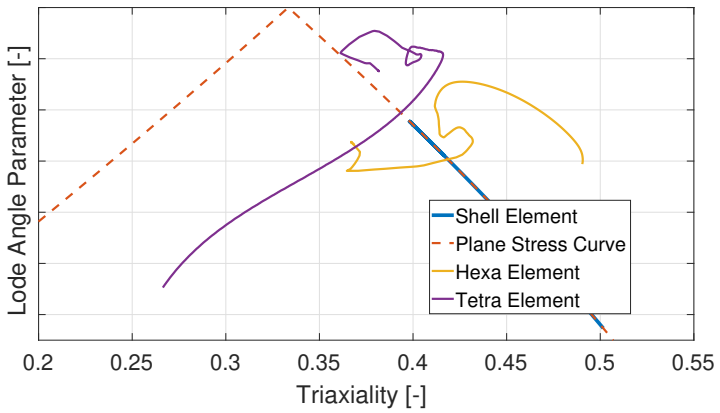

(a) Evolution of LAP with respect to triaxiality for hole medium (1 mm) coupon in CrachFEM. The critical shell, hexa, and tetra elements are plotted together with the plane stress curve.

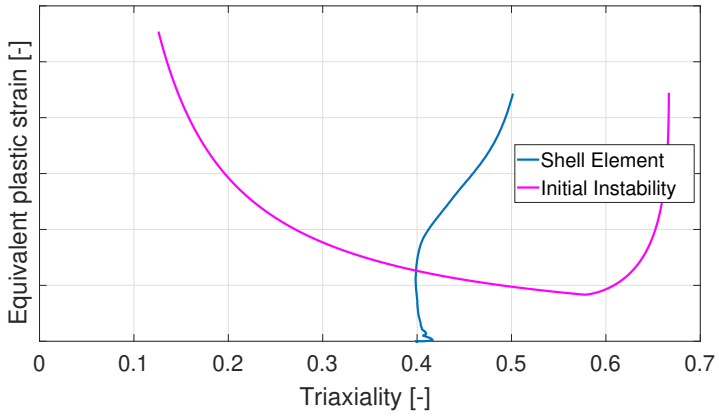

(b) Evolution of equivalent plastic strain with respect to triaxiality for hole medium (1 mm) coupon in CrachFEM. The critical shell element is plotted together with the initial instability curve.

Figure 4.15: Evolution of LAP vs. triaxiality, and evolution of equivalent plastic strain vs. triaxiality for the critical shell element for hole medium (1 mm) coupon.

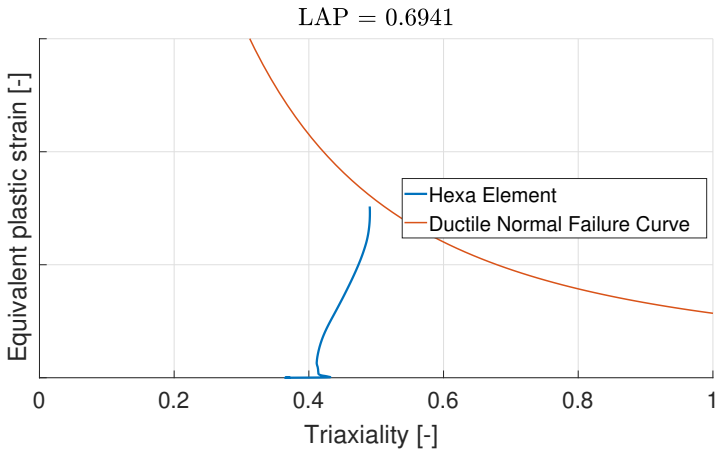

(a) Evolution of equivalent plastic strain with respect to triaxiality for hole medium (1 mm) coupon in CrachFEM. The critical hexa element is plotted together with its failure curve.

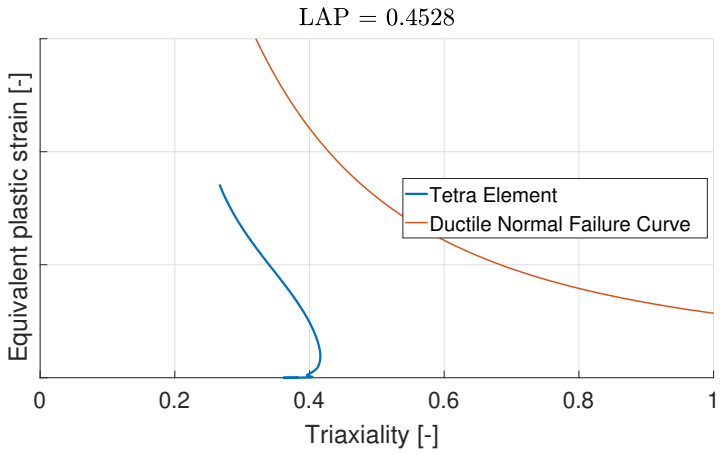

(b) Evolution of equivalent plastic strain with respect to triaxiality for hole medium (1 mm) coupon in CrachFEM. The critical tetra element is plotted together with its failure curve.

Figure 4.16: Evolution of equivalent plastic strain vs. triaxiality for the critical hexa and tetra elements for hole medium (1 mm) coupon.

When considering tetra elements there is another factor that gives the results an unreliable behaviour, and that is the volumetric locking effect, coming from that tetra elements have difficulties to accommodate the (nearly) incompressible deformation during plastic loading. In Fig. 4.17 it is clearly visible that the tetra elements have mismatched hydrostatic pressure compared to neighbouring elements in the critical areas, and this locking effect is not present for the hexa elements. Being limited to two elements in thickness gave the tetra elements bad aspect ratios, which would only get worse when the elements were being stretched. This created the inconsistent evolution of the triaxiality, most notably in Fig. 4.16(b) where the strain path moves away from the failure surface.

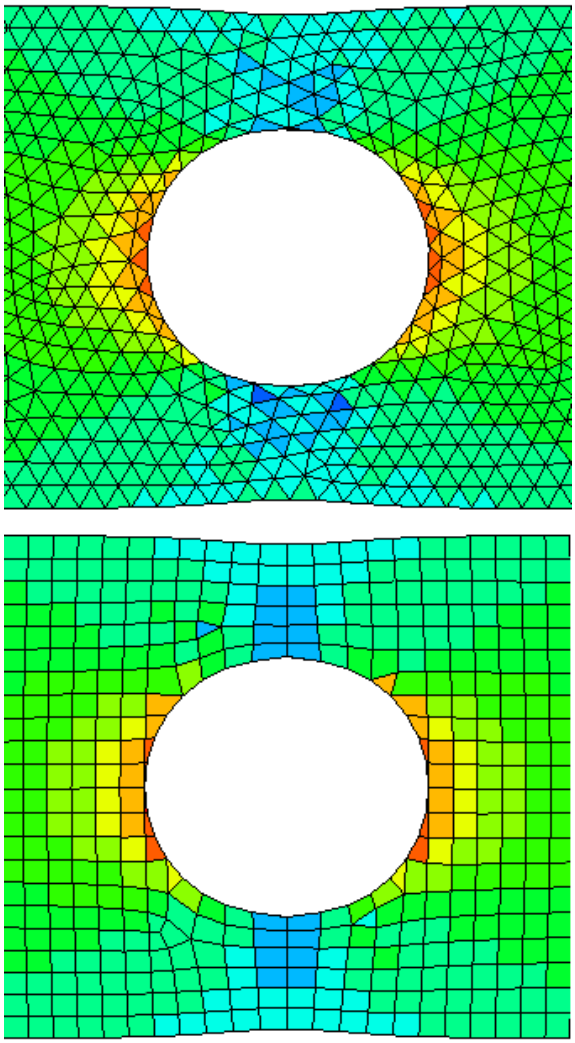

Figure 4.17: Surface plot of the hydrostatic pressure for the hole coupon with hexa and tetra elements in CrachFEM.

4.3 GISSMO

As mentioned before, GISSMO is a damage model in which different failure curves can be incorporated. In this section, different failure models are tested.

4.3.1 Sanity Check

The results from the sanity check, aimed at verifying the critical curve implementation, demonstrate that the outcomes from CrachFEM and the critical failure curve implemented in GISSMO are almost identical. This is evident in Fig. 3.8, as well as in Fig. 4.18, Fig. 4.19, and Fig. 4.20. This matching justifies a correct use of the beta and theta failure model in GISSMO.

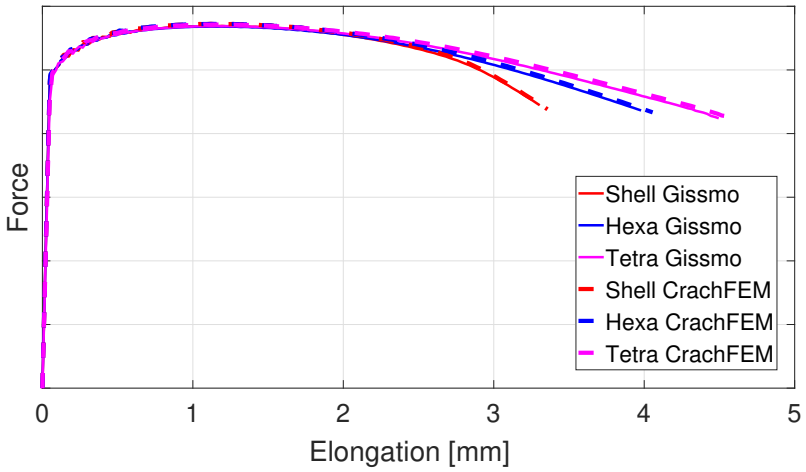

Figure 4.18: Comparison between CrachFEM and GISSMO for different element types in a tensile medium (1 mm) coupon test.

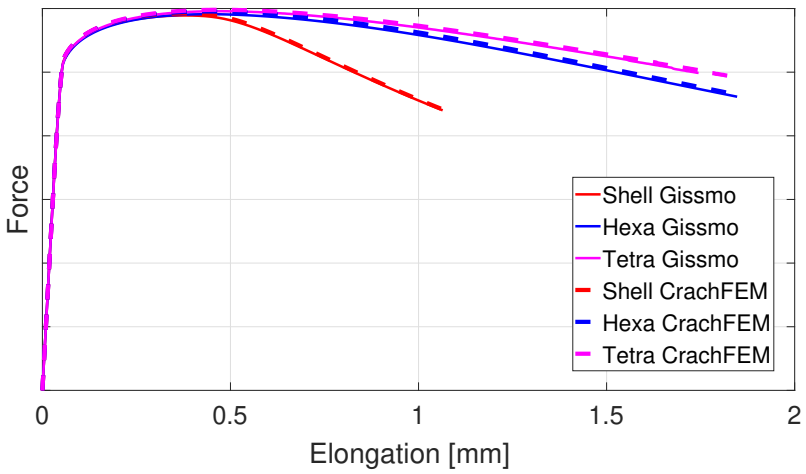

Figure 4.19: Comparison between CrachFEM and GISSMO for different element types in a waist medium (1 mm) coupon test.

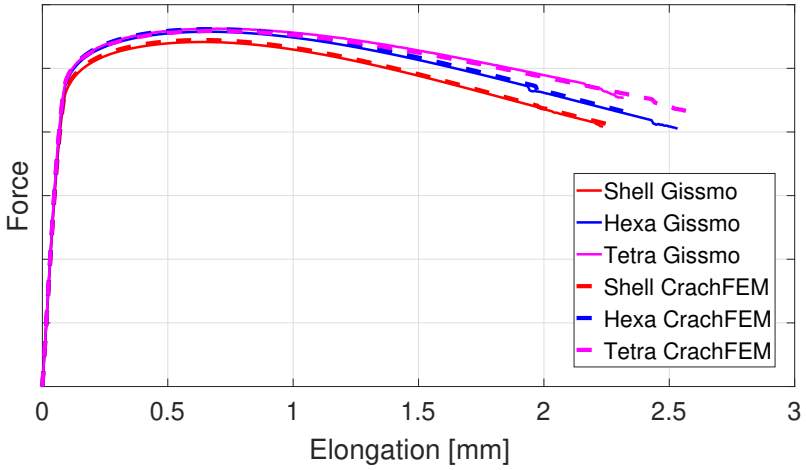

Figure 4.20: Comparison between CrachFEM and GISSMO for different element types in a hole medium (1 mm) coupon test.

4.3.2 Anisotropic Material with GISSMO

Introducing plastic anisotropy to match the anisotropic model in CrachFEM appears to be very effective, as the calibrated Barlat material model functions as intended. While there are some differences, particularly in the shell elements, the solid elements exhibit behavior that closely aligns with the expected results. This supports the use of the Barlat anisotropic material model in conjunction with the CrachFEM failure curve as seen in Fig. 4.21, Fig. 4.22, and Fig. 4.23.

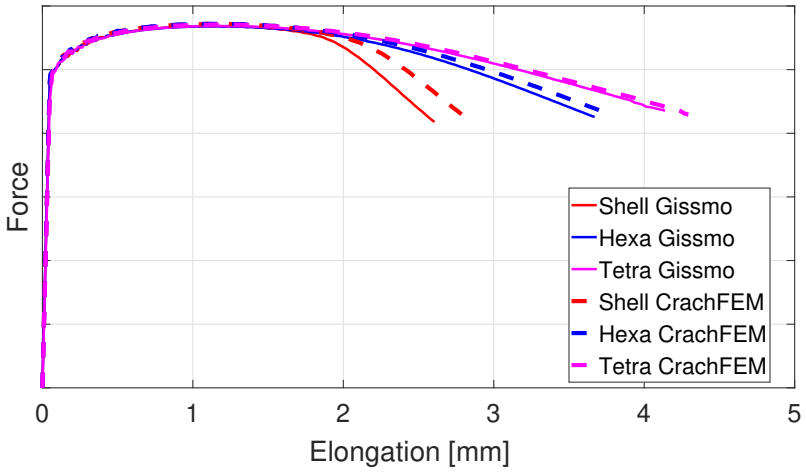

Figure 4.21: Comparison between CrachFEM and GISSMO for different element types in a tensile medium (1 mm) coupon test. Here the GISSMO model is considering plastic anisotropy.

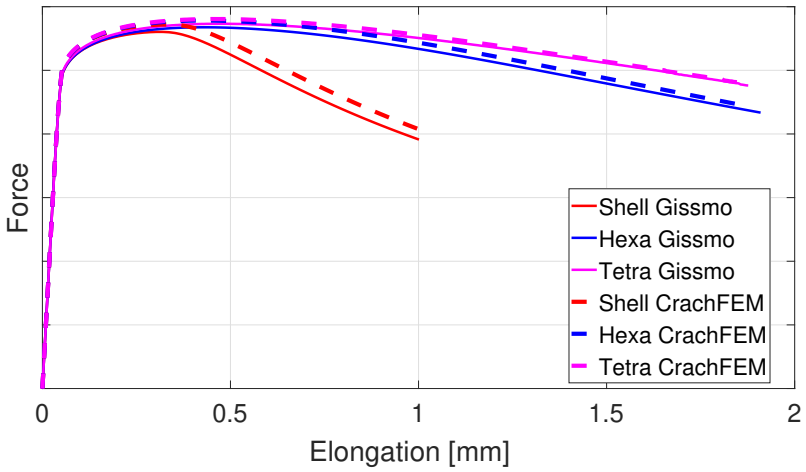

Figure 4.22: Comparison between CrachFEM and GISSMO for different element types in a waist medium (1 mm) coupon test. Here the GISSMO model is considering plastic anisotropy.

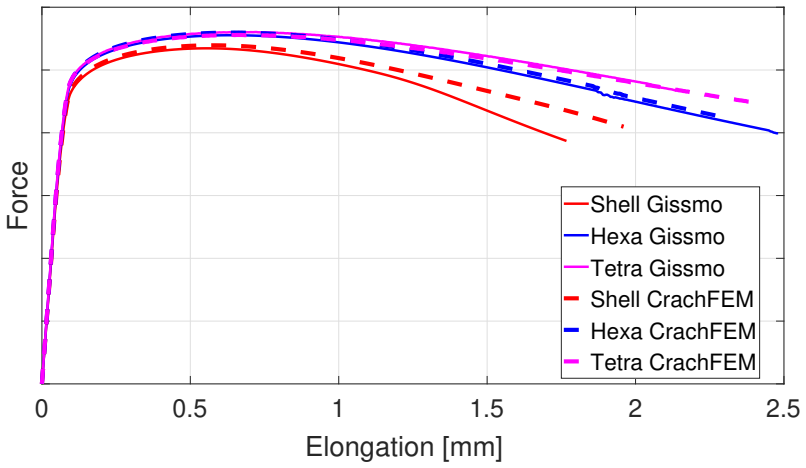

Figure 4.23: Comparison between CrachFEM and GISSMO for different element types in a hole medium (1 mm) coupon test. Here the GISSMO model is considering plastic anisotropy.

4.3.3 Regularization

The optimization of regularization parameters in LS-OPT gave the results shown in Table III. Using these parameters in GISSMO resulted in expected shifts to the force/displacement curves for the different mesh densities of hexa elements, similar to the shift in curves shown in Fig. 3.10. However, the tetra elements did not share this behaviour and barely shifted at all. This was because of how LS-DYNA defined the element lengths of hexas and tetras, effectively giving tetras a third of the element size which made them closer to the reference element length than they should have been. Additionally, the regularization was only made for the beta/theta model in GISSMO, the Cockcroft-Latham and MMC models did not use this function.

TABLE III
REGULARIZATION PARAMETERS

Mesh density	Parameter value
Finest mesh (0.2 mm)	1
Fine mesh (0.5 mm)	0.877177
Medium mesh (1 mm)	0.621689
Coarse mesh (3 mm)	0.456306

4.3.4 Studying the Effect of Damage and Fade Exponent & Incorporating Instability for 3D Solids

The effect of the damage exponent is illustrated in Fig. 4.24 and Fig. 4.25, where increasing the damage exponent enhances the plastic strain capacity, indicating that the specimen can elongate more. On the other hand, the effect of the fade exponent, shown in Fig. 4.26 and Fig. 4.27, decreases triaxiality development over time while simultaneously increasing the plastic strain capacity. The effect of the damage and fade exponent is tied to post-instability, as the effect can clearly be seen after reaching the initial instability curve.

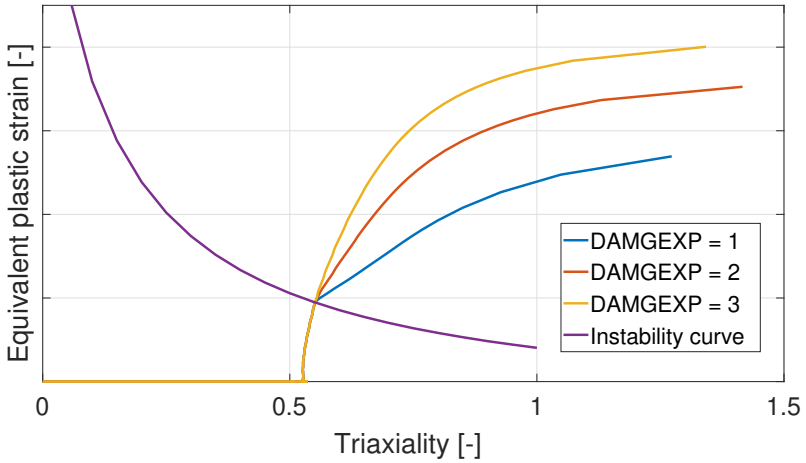

Figure 4.24: Effect of the DAMGEXP in the triaxiality vs equivalent plastic strain plane for a medium (1 mm) tensile coupon test with hexa elements in GISSMO.

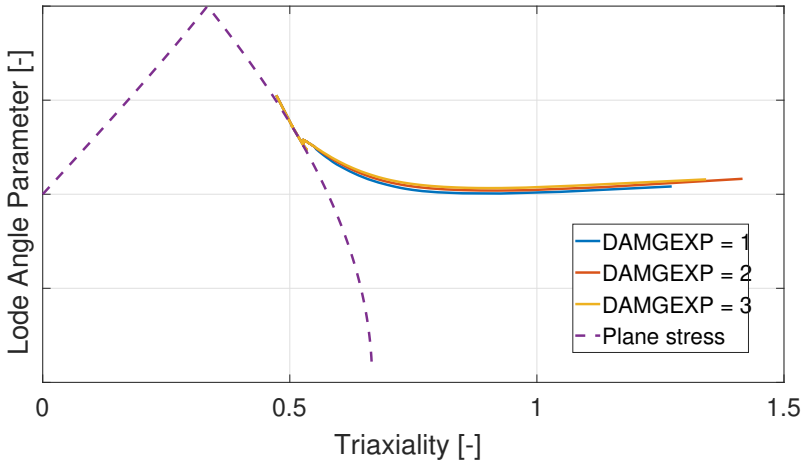

Figure 4.25: Effect of the DAMGEXP in the triaxiality vs LAP plane for a medium (1 mm) tensile coupon test with hexa elements in GISSMO.

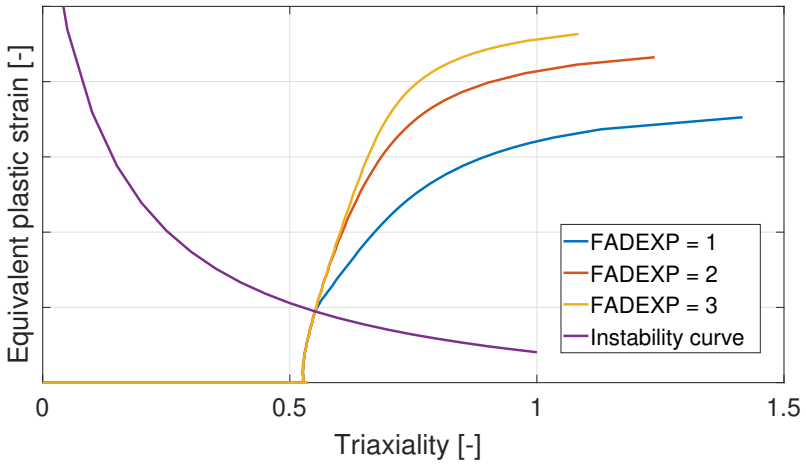

Figure 4.26: Effect of the FADEXP in the triaxiality vs equivalent plastic strain plane for a medium (1 mm) tensile coupon test with hexa elements in GISSMO.

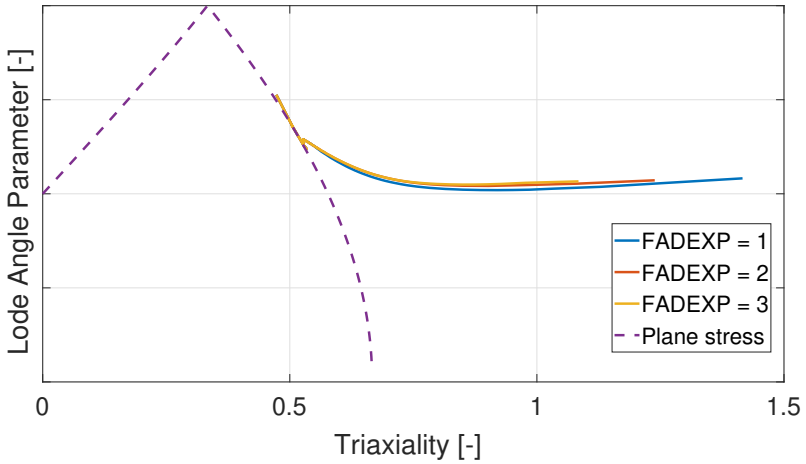

Figure 4.27: Effect of the FADEXP in the triaxiality vs LAP plane for a medium (1 mm) tensile coupon test with hexa elements in GISSMO.

Incorporating the instability described in (51) for solid elements results in behavior that more closely resembles that of shell elements when the appropriate settings for the damage exponent and fade exponent are used. This is demonstrated in Fig. 4.28 - Fig. 4.33. GISSMO provides more customizable results, allowing for better alignment with the desired reference behavior. The incorporation of instability for solid elements is primarily a mathematical expression, aimed at matching the behavior of experimental and shell elements. For shell elements, instability is introduced to induce failure due to necking, compensating for the lack of geometrical necking in these elements. Introducing extended instability for 3D solid elements as in section 2.5 within the GISSMO damage model shows capabilities for improving results. However, the settings employed in GISSMO are not uniform across the board at least for fade exponent. This inconsistency manifests in the use of varying fade exponents in an attempt to achieve a better fit with experimental data. While this approach may yield improved results, the lack of consistency in settings suggests that further refinement is necessary to ensure robustness and reliability in the model's predictive capabilities. A damage exponent of 3 consistently aligns with the experimental curves, providing reliable results. However, the fade exponent displays some variability across different coupons, making its value uncertain and subject to elimination.

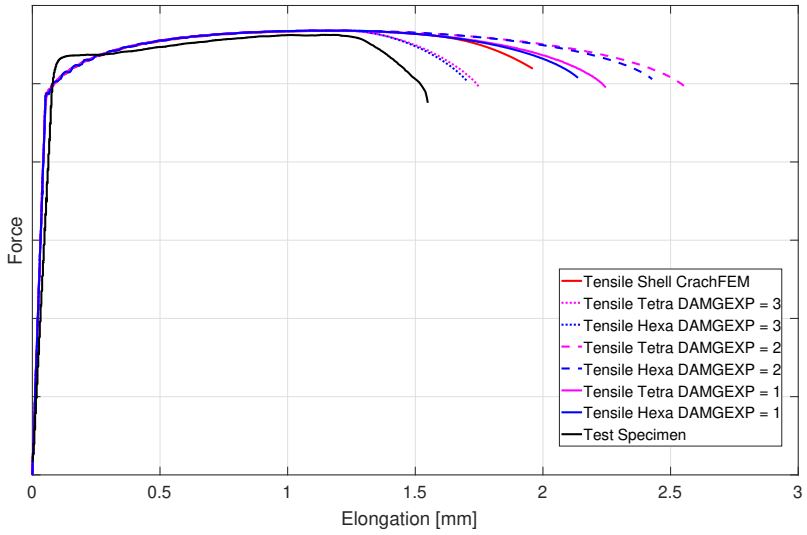

Figure 4.28: Comparison of various configurations with element types and DAMGEXP values for the GISSMO model with CrachFEM shell and test specimens for medium (1 mm) tensile tests.

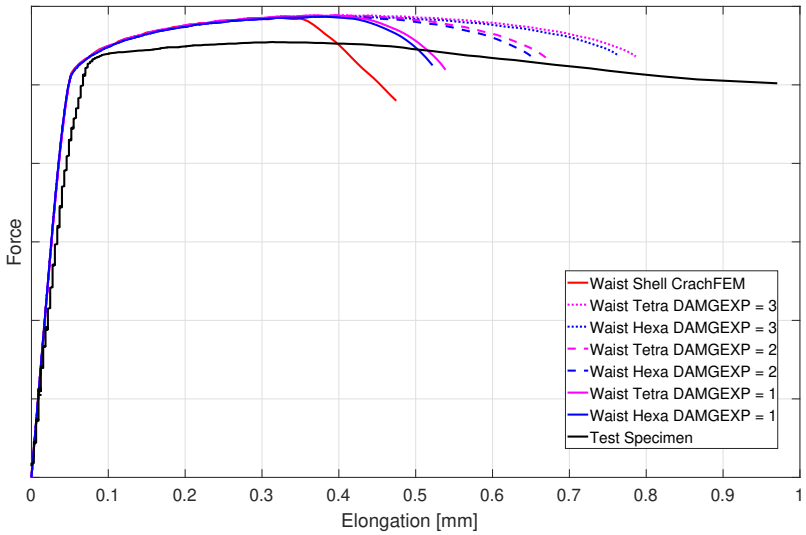

Figure 4.29: Comparison of various configurations with element types and DAMGEXP values for the GISSMO model with CrachFEM shell and test specimens for medium (1 mm) waist tests.

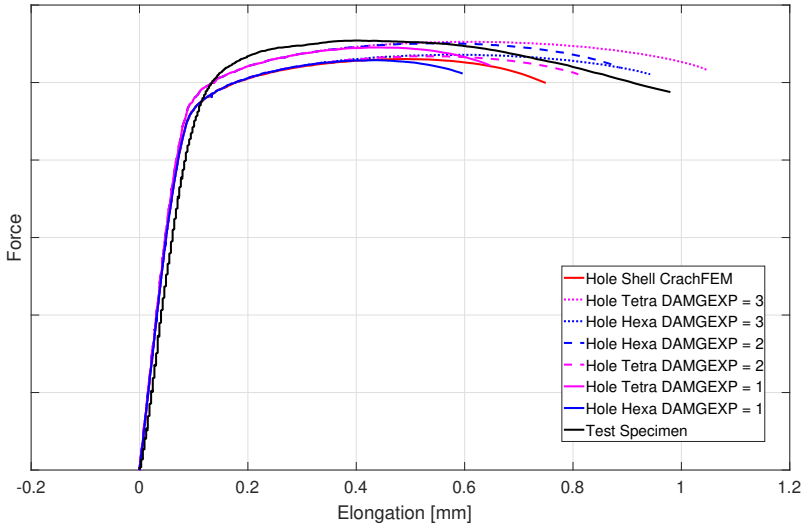

Figure 4.30: Comparison of various configurations with element types and DAMGEXP values for the GISSMO model with CrachFEM shell and test specimens for medium (1 mm) hole tests.

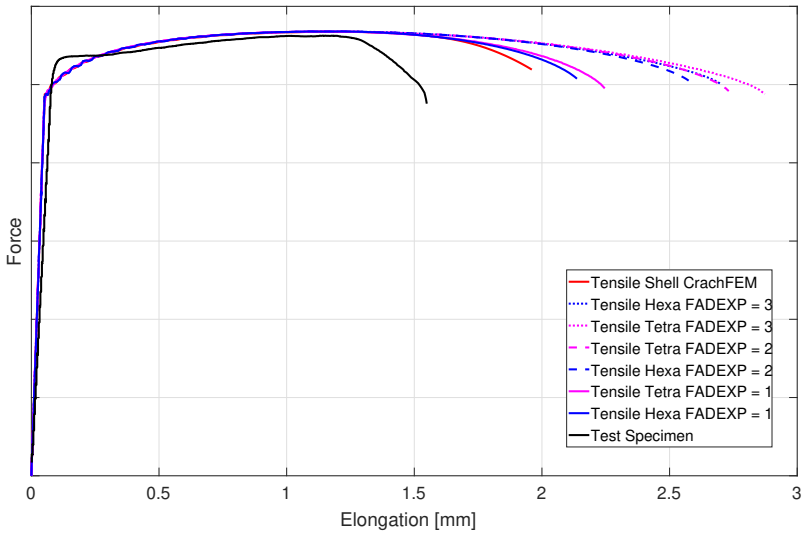

Figure 4.31: Comparison of various configurations with element types and FADEXP values for the GISSMO model with CrachFEM shell and test specimens for medium (1 mm) tensile tests.

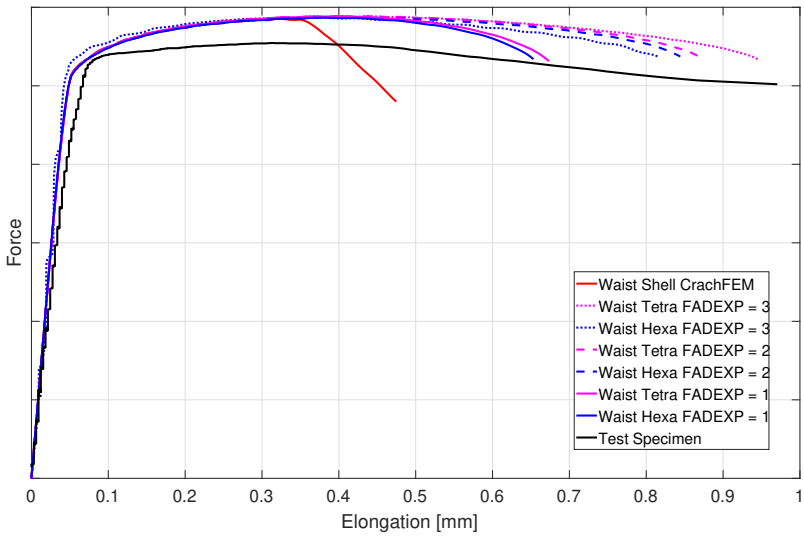

Figure 4.32: Comparison of various configurations with element types and FADEXP values for the GISSMO model with CrachFEM shell and test specimens for medium (1 mm) waist tests.

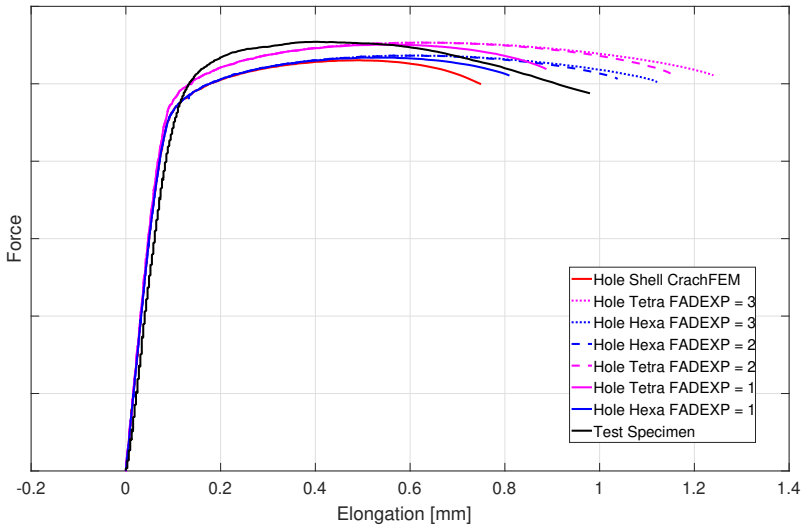

Figure 4.33: Comparison of various configurations with element types and FADEXP values for the GISSMO model with CrachFEM shell and test specimens for medium (1 mm) hole tests.

4.3.5 Cockcroft-Latham Using GISSMO

The results obtained from the Cockcroft-Latham failure model shown in Fig. 4.34 and Fig. 4.35 exhibit a superior alignment with experimental outcomes in terms of elongation level compared to the CrachFEM failure model, even without factoring in the extended instability failure. However, this alignment is not observed in Fig. 4.36, where there is a significant deviation between solid elements and experimental data. This discrepancy may be attributed to the fact that the Cockcroft-Latham failure model is calibrated based on regular tensile tests, hence its performance with other types of coupons may not be as expected indicating that there might be a problem for higher triaxiality. While it demonstrates some consistency with the waisted experimental data in terms of elongation level, its performance is inconsistent with coupons other than tensile coupons.

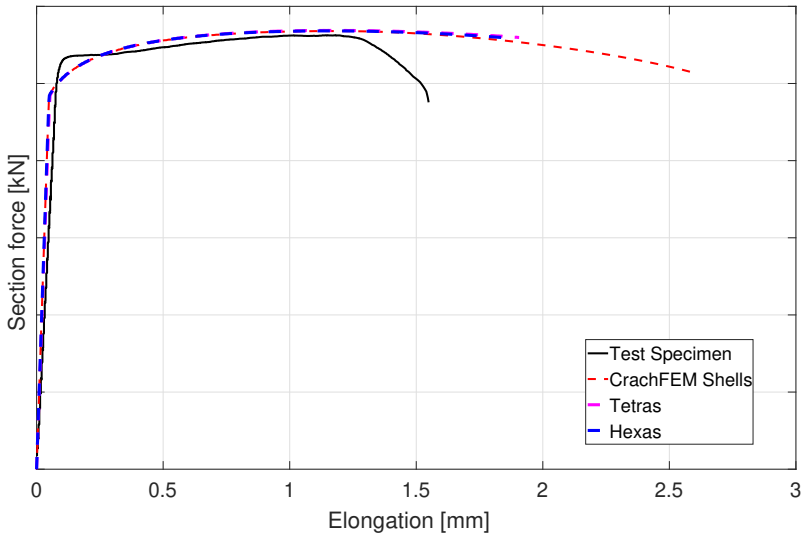

Figure 4.34: Cockcroft-Latham failure model applied to medium (1 mm) tension in GISSMO.

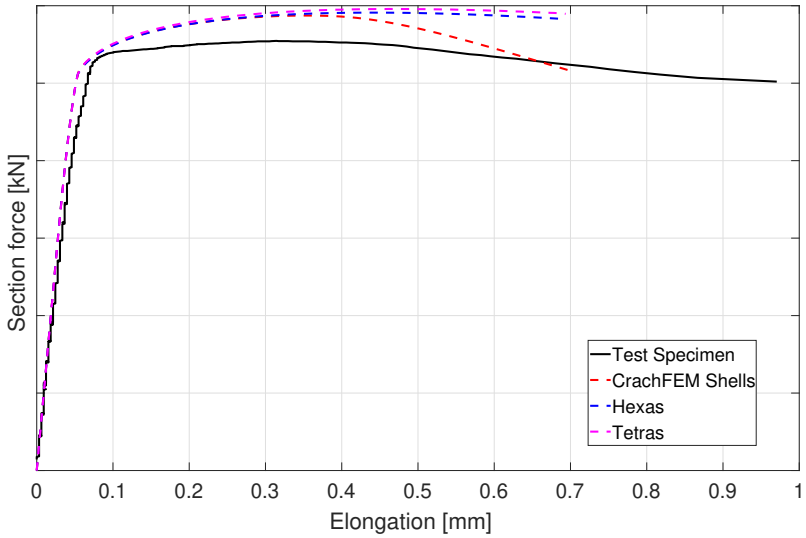

Figure 4.35: Cockcroft-Latham failure model applied to medium (1 mm) waisted coupon in GISSMO.

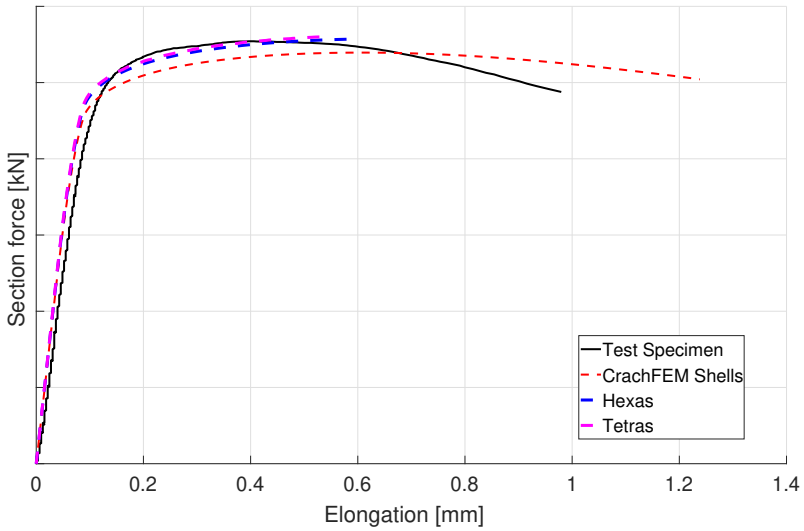

Figure 4.36: Cockcroft-Latham failure model applied to medium (1 mm) hole coupon in GISSMO.

4.3.6 Modified Mohr-Coulomb Using GISSMO

The MMC model demonstrates notable alignment in both force amplitude and elongation level when used for the medium tensile coupon, as evidenced by Fig. 4.37. However, this observed alignment may not extend to other types of coupons. For instance, the waisted coupon depicted in Fig. 4.38 exhibits a lack of correspondence with experimental results, while the hole coupon in Fig. 4.39 shows a more decent matching. It is important to note that further optimization of the MMC model could potentially yield even better outcomes. Nonetheless, it is evident that MMC exhibits superiority over both the CrachFEM and Cockcroft-Latham models.

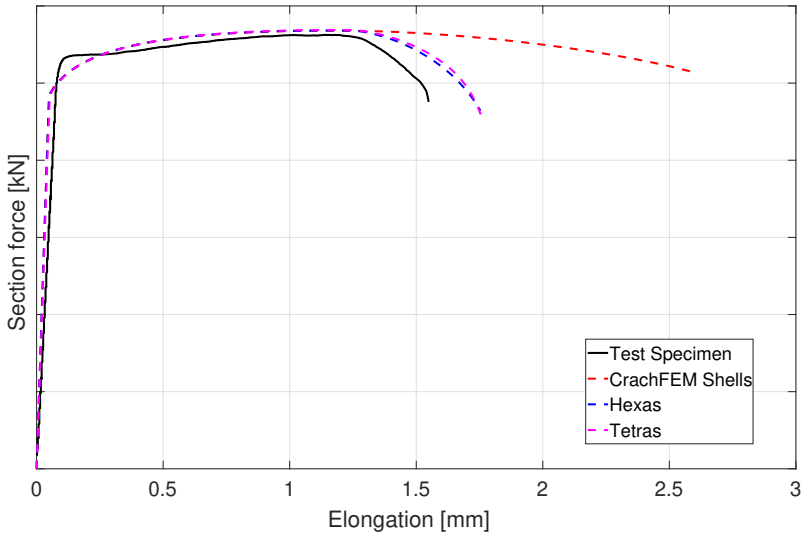

Figure 4.37: Modified Mohr-Coulomb failure model applied to medium (1 mm) tension coupon in GISSMO.

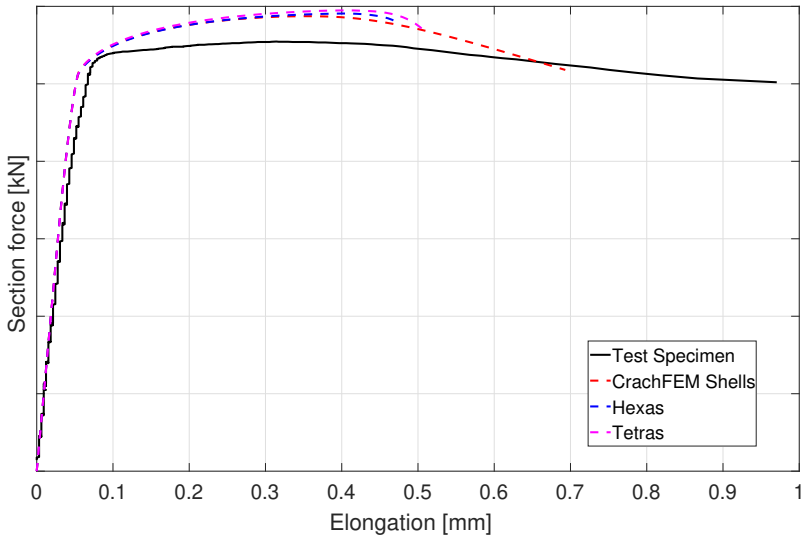

Figure 4.38: Modified Mohr-Coulomb failure model applied to medium (1 mm) waisted coupon in GISSMO.

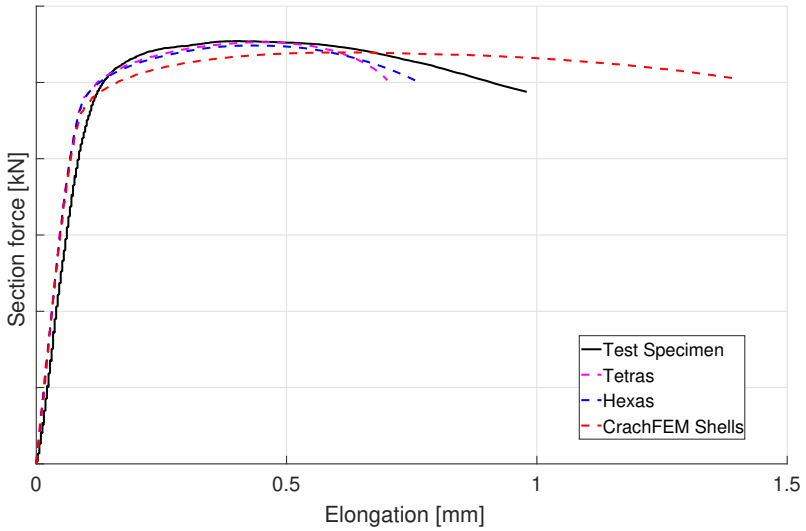

Figure 4.39: Modified Mohr-Coulomb failure model applied to medium (1 mm) hole coupon in GISSMO.

4.4 Component Simulation

The results from using the beta/theta models in CrachFEM and GISSMO for the component testing are shown in Fig. 4.40. Here, it is evident that all configurations of element type and mesh density overshoot the point of failure in elongation by a large amount. This is in accordance to the uniaxial tension test, in which this component test is most related to, since the three-point bending test had a groove in the middle. The general result here is that the GISSMO model is closer to the experimental data than CrachFEM. That is because the model is using the instability criterion, which was examined for the coupon tests.

The GISSMO result also showcases that the regularization is working as intended. All the different hexa configurations follow the same trend, but the tetras do not show the same results due to them not being affected as much by the regularization, as discussed in subsection 4.3.3. This highlights that regularization is needed to generate consistent results in more complex models with varying mesh densities.

Hexa elements have been shown to be the most consistent element type for CrachFEM and GISSMO. In both models the tetra elements using a medium mesh have a force magnitude that greatly exceeds all other curves. However, when refining the mesh density to fine, the tetra elements shift downwards in force magnitude and matches the hexa elements. However, refining is not a feasible option for uses in larger models, since for the component alone the tetra fine mesh consisted of about 26 million elements.

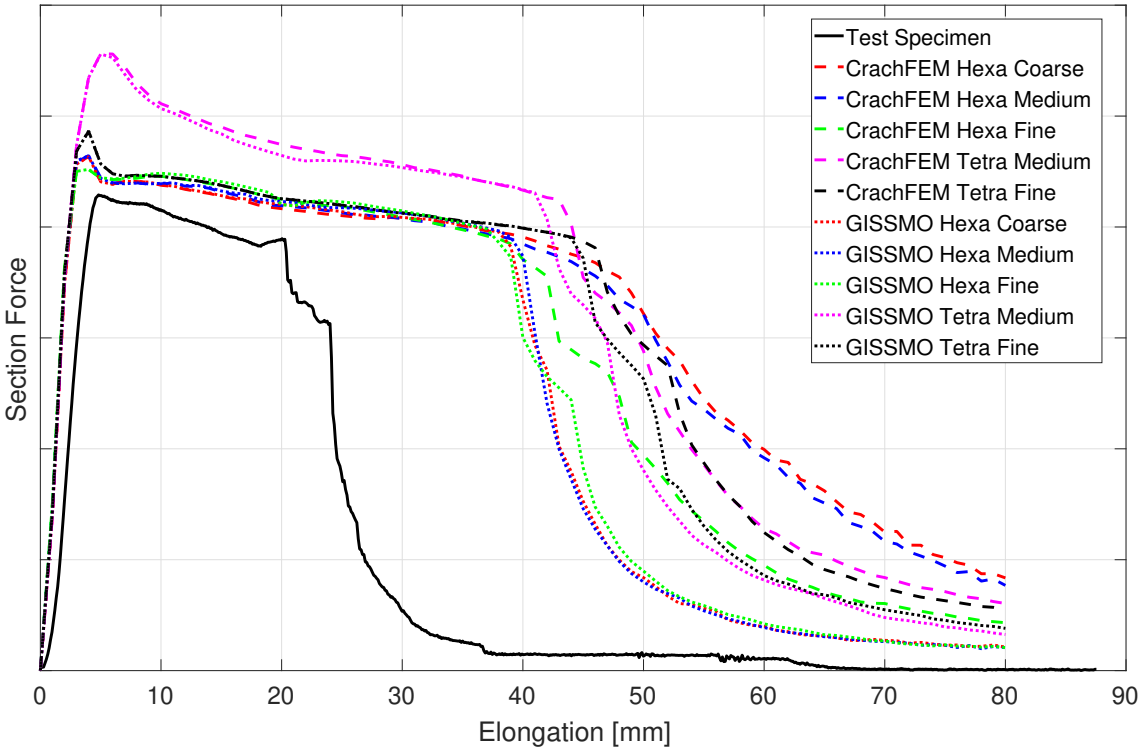

Figure 4.40: Evolution of the section force with respect to the elongation for the three point bending test of the component. Both the CrachFEM and GISSMO models with various element types are compared to the experimental test specimens.

Running the same simulation of the component using medium hexa and tetra with GISSMO using both the Cockcroft-Latham and MMC criteria gave results that showed much promise, as shown in Fig. 4.41. These results did not overshoot the point of failure in elongation as the beta/theta model did. Out of the two criteria the MMC matches the experimental data the best for hexa elements.

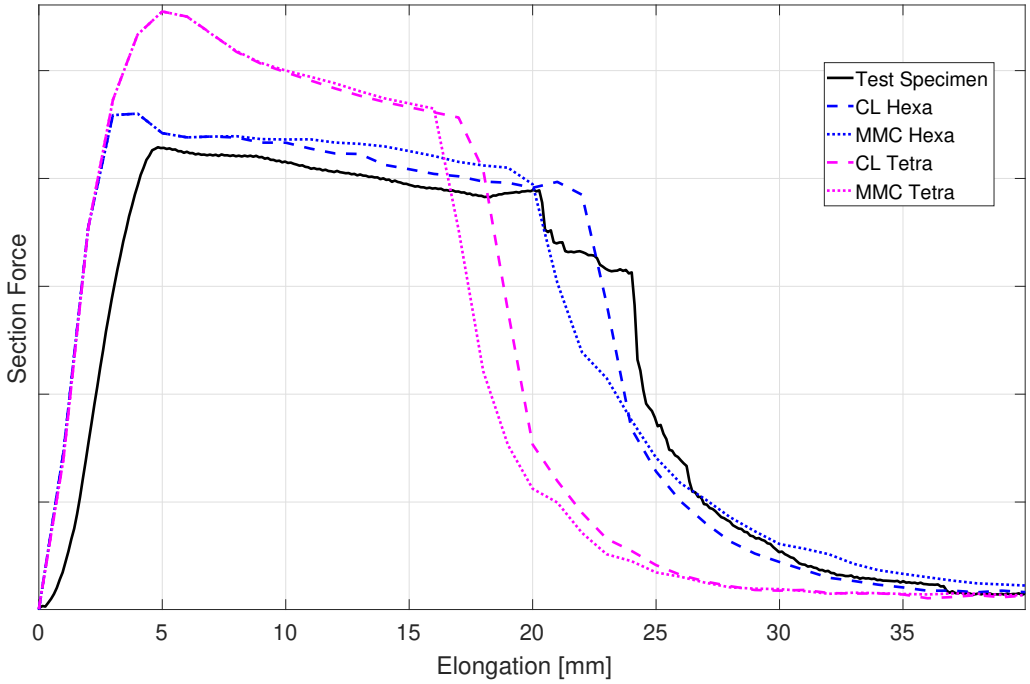

Figure 4.41: Evolution of the section force with respect to the elongation for the three point bending test of the component. Both the Cockcroft-Latham and Modified Mohr-Coulomb models incorporated in GISSMO are compared to the experimental test specimens.

5

Conclusion & Future Work

The project aimed to make an assessment of the CrachFEM material failure model to evaluate its validity for the use of 3D solid elements. The analysis was successfully conducted and it was found that CrachFEM by itself is insufficient for the use with 3D solid elements. This was found by comparing the various simulation results to experimental data. However, when instability was extended to 3D solid elements, and the beta/theta models were implemented into the material damage model GISSMO, the beta/theta models showed more promising results compared to experimental data. But there were difficulties finding values of the specific FADEXP parameters that would give consistent results between the different types of coupons as they are in tension.

In all models, the results obtained from shell elements and solid elements are significantly different. Therefore, it is crucial to use different calibration parameters for each type of model element. Using the same calibration for both shell and solid models is not recommended. This principle also extends to different types of solid elements. For instance, tetra and hexa elements likely require distinct calibration parameters to ensure accuracy in the results. This indicates the insufficiency of using a one-size-fits-all approach in modeling, highlighting the need for tailored calibration to account for the unique characteristics of each element type. Each element type has unique characteristics and behaviors that must be accounted for during the calibration process to achieve reliable and precise outcomes.

Cockcroft-Latham and MMC show better results than CrachFEM when they are simulated in the component test, though they are not perfect. Cockcroft-Latham as a failure surface is too simple as it does not change in value when moving along the LAP axis for constant triaxiality values, which resulted in inadequate results as demonstrated in Fig. 4.35 and Fig. 4.36. This model was calibrated for the use of uniaxial tension coupons. MMC seems to be a better model as it shows the most promising results when compared with physical component testing, shown in Fig. 3.13, but it requires further calibration and optimization to be fully extended to work for all various coupons.

Tetra elements, whether they are using the 1st or 2nd order element formulation, seem to be very hard to build a good and consistent mesh with. Even refining the mesh density to medium (1 mm) the tetra elements generated had bad aspect ratios which would only become worse as they were deformed in the tension tests.

Regularization in the GISSMO damage model is needed for more complex models, as it helps to give more consistent results when different mesh densities are used. It is also needed to reduce the amount of elements used in the model to lower the computational effort, since using anything finer than the coarse (3 mm) results in meshes with the number of elements in the millions.

In general, the main objectives of this project were conducted successfully. Different parts of the FE-solver were studied and analyzed to understand their contribution to the results and how these parts are different for shell and solid elements.

This project raised more questions for future work that are definitely needed to be studied and further analyzed. Mainly different types of coupons need to be tested to complete the full failure model for all types of load cases. Additionally, the results must be verified with different extruded aluminium types, beyond the one used in this project. Other points of work to be studied in the future include:

- To calibrate an advanced failure surface, based on additional tests, especially those that provide a triaxiality higher than 2/3.
- Optimize material parameters for the MMC failure criterion
- Study the tetra elements more extensively to understand their behaviour
- Study the 2nd order hexahedral elements
- Investigate other element formulations to complement the use of tetra elements
- Run more component tests with other configurations
- Improve regularization by isolating tetra and hexa elements in the optimization process

Bibliography

[1] B. Struthers, "Why aluminium in cars is common sense," *Shapes*, Jun. 2020. [Online]. Available: https://www.shapesbyhydro.com/en/material-properties/why-aluminium-in-cars-is-common-sense/.

[2] M. Tisza and I. Czinege, "Comparative study of the application of steels and aluminium in lightweight production of automotive parts," *International Journal of Lightweight Materials and Manufacture*, vol. 1, no. 4, pp. 229–238, 2018, ISSN: 2588-8404. DOI: https://doi.org/10.1016/j.ijlmm.2018.09.001. [Online]. Available: https://www.sciencedirect.com/science/article/pii/S2588840418300301.

[3] G. Liu and S. Quek, "Chapter 9 - fem for 3d solid elements," in *The Finite Element Method (Second Edition)*, G. Liu and S. Quek, Eds., Second Edition, Oxford: Butterworth-Heinemann, 2014, pp. 249–287, ISBN: 978-0-08-098356-1. DOI: https://doi.org/10.1016/B978-0-08-098356-1.00009-6. [Online]. Available: https://www.sciencedirect.com/science/article/pii/B9780080983561000096.

[4] N. Hashimoto, "Application of aluminum extrusions to automotive parts," *Kobelco Technology Review*, vol. 35, pp. 69–75, 2017.

[5] A. Graf, "Chapter 3 - aluminum alloys for lightweight automotive structures," in *Materials, Design and Manufacturing for Lightweight Vehicles (Second Edition)*, ser. Woodhead Publishing in Materials, P. Mallick, Ed., Second Edition, Woodhead Publishing, 2021, pp. 97–123, ISBN: 978-0-12-818712-8. DOI: https://doi.org/10.1016/B978-0-12-818712-8.00003-3. [Online]. Available: https://www.sciencedirect.com/science/article/pii/B9780128187128000033.

[6] M. Cockcroft and D. Latham, *Ductility and the Workability of Metals*. 1968. [Online]. Available: https://books.google.se/books?id=COSPAQAACAAJ.

[7] Y. Bai and T. Wierzbicki, "Application of extended mohr–coulomb criterion to ductile fracture," *International Journal of Fracture*, vol. 161, pp. 1–20, 2010, ISSN: 1573-2673. DOI: 10.1007/s10704-009-9422-8. [Online]. Available: https://doi.org/10.1007/s10704-009-9422-8.

[8] Y. Lou, H. Huh, S. Lim, and K. Pack, "New ductile fracture criterion for prediction of fracture forming limit diagrams of sheet metals," *International Journal of Solids and Structures*, vol. 49, no. 25, pp. 3605–3615, 2012, New Challenges in Mechanics Materials for Sheet Metal Forming, ISSN: 0020-7683. DOI: https://doi.org/10.1016/j.ijsolstr.2012.02.016. [Online]. Available: https://www.sciencedirect.com/science/article/pii/S002076831200056X.

[9] Y. Lou and H. Huh, "Evaluation of ductile fracture criteria in a general three-dimensional stress state considering the stress triaxiality and the lode parameter," *Acta Mechanica Solida Sinica*, vol. 26, pp. 642–658, Dec. 2013. DOI: 10.1016/S0894-9166(14)60008-2.

[10] Inwind, *File:cauchy stress t.svg*, This work is licensed under the Creative Commons Attribution 3.0 International License. To view a copy of this license, visit https://creativecommons.org/licenses/by-sa/3.0/., Aug. 2009. [Online]. Available: https://en.wikipedia.org/wiki/File:Cauchy_stress_t.svg.

[11] Sanpaz, *File:stress transformation 3d.svg*, This work is licensed under the Creative Commons Attribution 3.0 International License. To view a copy of this license, visit https://creativecommons.org/licenses/by-sa/3.0/., Jan. 2009. [Online]. Available: https://commons.wikimedia.org/wiki/File:Stress_transformation_3D.svg.

[12] D. Mohr and S. J. Marcadet, "Micromechanically-motivated phenomenological hosford–coulomb model for predicting ductile fracture initiation at low stress triaxialities," *International Journal of Solids and Structures*, vol. 67-68, pp. 40–55, 2015, ISSN: 0020-7683. DOI: https://doi.org/10.1016/j.ijsolstr.2015.02.024. [Online]. Available: https://www.sciencedirect.com/science/article/pii/S0020768315000700.

[13] Y. Bai and T. Wierzbicki, "A new model of metal plasticity and fracture with pressure and lode dependence," *International Journal of Plasticity*, vol. 24, no. 6, pp. 1071–1096, 2008, ISSN: 0749-6419. DOI: https://doi.org/10.1016/j.ijplas.2007.09.004. [Online]. Available: https://www.sciencedirect.com/science/article/pii/S0749641907001246.

[14] K. Danas and P. Ponte Castañeda, "Influence of the lode parameter and the stress triaxiality on the failure of elasto-plastic porous materials," *International Journal of Solids and Structures*, vol. 49, no. 11, pp. 1325–1342, 2012, ISSN: 0020-7683. DOI: https://doi.org/10.1016/j.ijsolstr.2012.02.006. [Online]. Available: https://www.sciencedirect.com/science/article/pii/S0020768312000467.

[15] B. Erice and F. Gálvez, "A coupled elastoplastic-damage constitutive model with lode angle dependent failure criterion," *International Journal of Solids and Structures*, vol. 51, no. 1, pp. 93–110, 2014, ISSN: 0020-7683. DOI: https://doi.org/10.1016/j.ijsolstr.2013.09.015. [Online]. Available: https://www.sciencedirect.com/science/article/pii/S0020768313003703.

[16] Nicoguaro, *File:stress strain ductile.svg*, This work is licensed under the Creative Commons Attribution 4.0 International License. To view a copy of this license, visit https://creativecommons.org/licenses/by-sa/4.0/., May 2020. [Online]. Available: https://commons.wikimedia.org/wiki/File:Stress_strain_ductile.svg.

[17] H. Swift, "Plastic instability under plane stress," *Journal of the Mechanics and Physics of Solids*, vol. 1, pp. 1–18, Oct. 1952. DOI: 10.1016/0022-5096(52)90002-1.

[18] H. Dell, H. Gese, and G. Oberhofer, *MF GenYld + CrachFEM 4.3 Users' Manual Theory*, Oct. 2018.

[19] LS-DYNA, *LS-DYNA Theory Manual Material Models Material Model 36: Barlat's 3-Parameter Plasticity Model*, 2006. [Online]. Available: https://lsdyna.ansys.com/wp-content/themes/lsdyna/dynamat/pdfs/mat_036_theory.pdf.

[20] S. Muftu, "Chapter 8 - rectangular and triangular elements for two-dimensional elastic solids," in *Finite Element Method*, S. Muftu, Ed., Academic Press, 2022, pp. 257–291, ISBN: 978-0-12-821127-4. DOI: https://doi.org/10.1016/B978-0-12-821127-4.00006-2. [Online]. Available: https://www.sciencedirect.com/science/article/pii/B9780128211274000062.

[21] M. Ristinmaa and N. Ottosen, *The mechanics of constitutive modeling*, en. London, England: Elsevier Science, Sep. 2005.

[22] *MF GENYLD + CRACHFEM*, https://www.matfem.de/crachfem.html, Accessed: 2024-02-16.

[23] T. Borrvall, "A general damage initiation and evolution model (diem) in ls-dyna," Jan. 2013.

[24] T. B. Stoughton and X. Zhu, "Review of theoretical models of the strain-based fld and their relevance to the stress-based fld," *International Journal of Plasticity*, vol. 20, no. 8, pp. 1463–1486, 2004, ISSN: 0749-6419. DOI: https://doi.org/10.1016/j.ijplas.2003.11.004. [Online]. Available: https://www.sciencedirect.com/science/article/pii/S0749641903001591.

DEPARTMENT OF INDUSTRIAL AND MATERIALS SCIENCE
CHALMERS UNIVERSITY OF TECHNOLOGY
Gothenburg, Sweden
www.chalmers.se

CHALMERS
UNIVERSITY OF TECHNOLOGY